The Pennsylvania State University

The Graduate School

# IMPACT OF PARTICLE LAYER BUILDUP ON THE MODELING OF HEAT TRANSFER FOR HIGH REYNOLDS NUMBER PARTICLE-LADEN FLOW

A Thesis in

Mechanical Engineering

by

Zachary D. Vickerson



Submitted in Partial Fulfillment

of the Requirements

for the Degree of

Master of Science

December 2021

The thesis of Zachary Vickerson's was reviewed and approved by the following:

Robert Kunz
Professor of Mechanical Engineering
Thesis Advisor

Michael Manahan
Assistant Research Professor of Mechanical Engineering

Mary Frecker
Professor of Mechanical Engineering
Head of Mechanical Engineering Department

# ABSTRACT

The heat transfer performance of a particle-laden flow has design implications for a wide range of industries. The objective of this thesis is to improve a previously proposed Eulerian CFD model for the heat transfer of a highly mass loaded high Reynolds number particle-laden flow. Experimentation had shown that a layer of copper particles accumulated on the bottom of the flow channel. The previous two field (gas + dispersed particle) model was extended to include a third field to represent this particle layer. Mass transfer models were developed to account for the deposition of particles from dispersed to particle layer and from particle layer back to dispersed. New drag and heat transfer models were developed to account for the interaction of the particle layer field with the core gas flow. The model is tested and implemented using NPHASE, an Eulerian Multiphase flow CFD solver, and suggestions for improvement are proposed.

**Keywords:** Multiphase Flow, Heat Transfer, Computational Fluid Dynamics, Particle Transport

# Table of Contents

# LIST OF FIGURES

# LIST OF TABLES

# LIST OF SYMBOLS

**Nomenclature**

| | | | |
|---|---|---|---|
| $a$ | Speed of Sound | $\mathrm{Nu}^{p,l}$ | Ranz Marshall Correlation Nusselt Number |
| A | Cell cross sectional area | | |
| $\mathrm{C_D}$ | Drag Coefficient | p | Pressure |
| $\mathrm{C_P}$ | Specific Heat | P | Turbulence Production |
| $\mathrm{C}_\mu, \mathrm{C}_{\omega 1}, \mathrm{C}_{\omega 2}$ | Turbulence Model Constants | Pr, $\mathrm{Pr}_t$ | Laminar and Turbulence Prandtl Numbers |
| $\mathrm{C_{TD}}$ | Turbulent Dispersion Constant | q | Turbulent Velocity Scale($\sqrt{\mathrm{k}}$) |
| d, $\mathrm{d}^p$ | Pipe, Particle Diameter | $\mathrm{q}''_w, \dot{\mathrm{q}}_w$ | Wall Heat Flux and Power |
| $\mathrm{D}^{kl}$ | Drag Interfacial Force Kernel | $\mathrm{Q}^{kl}$ | Interfacial Heat Transfer |
| | | Re | Reynolds Number |
| $D$ | Pipe Inner Diameter | $S^*$ | Shields Number |
| E | Law of the Wall Constant | $S_c$ | Critical Shields Number |
| $\mathrm{g}_i$ | Gravity Vector | SL | Solids Loading Ratio |
| h | Particle film thickness | St | Stokes Number |
| $\mathrm{h^k}$ | Specific Enthalpy | T | Temperature, shear per unit velocity |
| $H$ | Local heat transfer coefficient | $\mathrm{u}_i$ | Velocity |
| $\mathrm{J}^d$ | Gradient diffusion | $\mathrm{u}_\tau$ | Friction Velocity |
| k | Turbulent Kinetic Energy, thermal conductivity | $\mathrm{U}^+$ | Dimensionless Velocity in Log-Law |
| $k^l$ | Thermal conductivity of the film (liquid) | \|V\| | Velocity Magnitude |
| | | x | Axial Distance |
| L | Pipe Length | $\mathrm{y}^+$ | Non-dimensional Distance to Wall |
| $\dot{\mathrm{m}}$ | Mass Flow Rate | | |
| M | Mach Number | ∀ | Cell volume |
| $\mathrm{M}_{kl}$ | Turbulence Dispersion Interfacial Force | $\mathrm{u}^{c+}$ | Non-dimensional log layer velocity |

**Greek Symbols**

| | | | |
|---|---|---|---|
| α | Volume Fraction | $\mu, \mu_t$ | Molecular, Turbulent Viscosity |
| $\Gamma^{kl}$, $\Gamma^{lk}$ | Mass transfer from phase $k$ to $l$ and from phase $l$ to $k$ | ρ | Density |
| | | $\tau$ | Shear stress |
| $\delta_{\mathrm{ij}}$ | Kronecker Delta | $\sigma_q, \sigma_\omega$ | Turbulent Prandtl Numbers |
| $\Delta_{\mathrm{w}}$ | Wall Distance | ω | Specific Dissipation Rate |
| κ | Kolmogorov Constant | | |
| λ | Thermal Conductivity | | |

**Subscripts/Superscripts**

| | | | |
|---|---|---|---|
| i, j | Cartesian Tensor Components | $p$ | Particle |
| | | $P$ | Cell Center Adjacent to Wall |
| $k, l$ | Phase Indicators | | |
| $l$, $g$ | Particle film phase(modeled as liquid), gas phase | $r$ | Relative |
| | | $sys$ | System Value |
| $m$ | Mean Value | $t$ | Turbulent Quantity |
| $f$ | Fluid Value | $w$ | Wall Value |

# ACKNOWLEDGEMENTS

Firstly, I would like to sincerely thank my advisor Dr. Robert Kunz, without whom this Thesis would not have been possible. His guidance carried me through all stages of this Thesis process and he provided a much-needed voice of reason when times grew stressful. It has been an honor working with him.

I would also like to thank Dr. Catherine Berdanier. Her work as the director of online programs did not go unnoticed, and the fact that I was able to complete a Masters of Science in Mechanical Engineering with a thesis component while working for the Navy in South Carolina is a testament to the excellent work she does. I would be remiss if I did not mention that this Thesis in particular benefited greatly from Dr. Berdanier's academic writing course.

To all the wonderful faculty and staff at Pennsylvania State University, I say thank you. I have nothing but amazing things to say about every professor and administrator I worked with these past three years. I've learned so much, and I would not trade this experience for anything.

Finally, I would like to thank my wife, Caroline Vickerson. She put up with all my late nights studying and always had a word of encouragement for me. Without her love and support I would never have completed this thesis.

# Chapter 1 Literature Review

Researchers have long studied the behavior of a flowing gas or liquid with suspended solid particles. These flows, more commonly referred to as particle-laden flows, have uses in a wide range of industries from nuclear reactor cooling to combustion. In many cases, the thermal performance of the flow factors significantly into the design of the system, such as for a pneumatic transport reactor. A pneumatic transport reactor improves the efficiency of a chemical reaction by transporting a suspension of the reacting particle through the reactor by means of a gas. Finely tuned control of the temperature throughout the reactor could improve the yield of the reaction, showcasing the importance of the heat transfer characteristics of the particle-laden flow [1,2]. Other applications for particle-laden flows, such as nuclear reactor cooling and metallic combustion systems, direct the flow through a heat exchanger[3]. Improving the heat transfer performance of a flow through the addition of particles could improve heat transfer rates without increasing the size of the heat exchanger [4].

Often, particle-laden flows operate at high Reynolds numbers, the focus of the current modelling work. The objective of this thesis is to improve the fidelity of a computational fluid dynamics (CFD) model for high Reynolds number particle-laden flows, originally proposed by Hassan et al. [5], by properly accounting for the impact of settling copper particles.

A literature review is presented here, which provides an overview of the major findings from studies on particle-laden flow heat transfer since 1957. The focus will then

shift to a recent experimental study on high Reynolds number flows conducted by Masters [6], which formed the basis of Hassan et al.'s [5] CFD analysis. The review will conclude by discussing research on particle transport as it applies to the current work.

## Nusselt Number in Two-Phase Flow

The Nusselt number, the ratio of convective over conductive heat transfer ($Nu = \frac{h\,D}{k}$), is a useful metric to compare the heat transfer characteristics of various flows. While researchers have developed accurate empirical correlations for the Nusselt number in single-phase flows [7–9], the addition of solid particulates in the two-phase flow of interest in this thesis complicates the behavior of convection heat transfer and thereby the Nusselt number, and indeed invalidates single-phase correlations. Existing research has focused on identifying the various factors that impact the heat transfer performance of two-phase flow. Researchers have studied the effect of the solids loading ratio [2,4,10–15], particle size [10–12,16], and the solids heat capacity [15,17–19] on the heat transfer performance for two-phase flows.

Researchers have established that the addition of solid particles can either increase or decrease the heat transfer effectiveness of a flow. Farbar and Morley [4] studied the flow of a gas-solids mixtures in circular tubes and found that the Nusselt number increased with solid loading. In contrast, a similar study conducted by Depew [12] found that the Nusselt number decreased up to a specific loading ratio and then increased thereafter. Later studies corroborated this finding [11,13,16], and researchers strove to understand the mechanism for this behavior. Boothroyd and Hague [16] suggested the addition of particles could suppress the turbulence within the flow leading to a reduction in the convective heat transfer. Succeeding works done by Kane and

Pfiefer [13], Han et al. [17], and Liu et al. [18] all suggested that the suppression of heat transfer led to the thickening of the viscous sublayer. As the viscous sublayer does not transfer heat as effectively, this leads to a reduction in the Nusselt number for low solid loadings.

Particle size also plays an important role in the heat transfer characteristics of a particle-laden flow. Depew and Farbar [11] tested two particle sizes, 30 microns and 200 microns, and observed no significant differences in the Nusselt number between these cases. Similarly, Han et al. [17] observed that larger particle sizes fail to enhance the Nusselt number. Boothroyd and Hague [16] attributed this result to turbulent eddies in the flow, which aide convective heat transfer, being unable to transport larger particles.

Several researchers have determined that the heat capacity of the solid particle also has a significant impact on the heat transfer performance. Han et al. [17] introduced the heat capacity-density product ratio as a means of further explaining the behavior of the Nusselt number observed by earlier works. This ratio, which is the product of the density and the heat capacity for the particulate phase over the gaseous phase, accounts for the increase in heat transfer one would expect from adding a material with a high heat transfer capacity. In agreement with earlier studies, the group observed that the thickening of the viscous sublayer is dominant at low solids loadings. However, the study proposed that as the loading ratio increases, the sublayer thickness does not significantly change, and the heat capacity-density product ratio dominates leading to an enhancement of heat transfer. This finding was further supported through a recent study by Liu et al. [18] who found that while adding particles with low specific heat led to heat transfer reduction, particles with high specific heat enhanced the heat transfer.

## High Reynolds Number Studies

While some investigators have established that solids loading ratio, particle size, and particle heat capacity affect heat transfer, most studies focus on Reynolds numbers less than $3x10^4$. Two of the only prior studies exploring higher Re regimes was that of Masters' experimental study [6], and Hassan et al.'s modeling work [5], on which the present research is based.

Masters' [6] thesis detailed a study to determine the effect of particle concentration and Reynolds number on the heat transfer for particle-laden flows and observed that an optimal Reynolds number exists for maximum heat transfer. They studied Reynolds numbers ranging from $3x10^4 – 6x10^4$, and compared measured Nusselt number for three solids loading ratios, where the solids loading ratio was defined as the mass flow rate of solids divided by the mass flow rate of gas. Masters found that for each solid loading ratio, there were ranges of Reynolds numbers that exhibited either reduced or enhanced heat transfer compared to the gas only flows, but all solids loading ratio's tested experienced a peak in Nusselt number within the Reynolds number range tested of $3x10^4$ and $6.5x10^4$. Masters concluded that while further study using different solids loading ratios could help build a more complete picture, it was clear that the heat transfer performance of the flow was augmented under certain conditions.

Beyond the experimental work at high Reynolds regimes, some workers have attempted to develop predictive models for particle laden flow heat transfer. Hassan et al. [5] developed a CFD model for the high Reynolds number particle laden flow in Masters' [6] thesis. The model performed reasonably well at the higher Reynolds numbers, but unsatisfactory errors were observed at a Reynolds number of $3x10^4$. They suggested that

these errors could stem from inaccurate modeling of the particle distribution within the flow. Their model accounted for gravity, drag, and turbulence dispersion using well established correlations [20,21], however the impact of particles depositing on the bottom of the flow channel was not considered. This thesis extends the CFD models presented in Ref. [4] by modeling the impact of this particle layer along the bottom of the flow channel with the goal of reducing the errors observed in Ref. [4].

## Saltation Background

The phenomenon of saltation, the predominant mode of transport for small particles exposed to a flowing fluid, has been studied since the early 1900s [22], and has since been the focus of foundational quantitative and qualitative research [23]. Classically, saltation has been used to describe the skipping motion of sand particles as they are picked up by the wind and continually rebound off the surface [24]. For the present study, there are several elements of saltation fluid mechanics that have particular relevance; the saltation velocity, the concentration profile, the mass flux of particles in the saltation layer, and the rate of re-entrainment of saltating particles. These will be discussed in greater detail in the following paragraphs.

Saltation velocity, the minimum velocity required to keep particles in suspension without settling [25], is an important area of research for channel flows and pipe flows, such as the flow of interest in this thesis. Several researchers have derived equations to calculate the saltation velocity for various flows. Jones and Leung [26] evaluated eight different saltation velocity correlations and determined that the Rizk [27] correlation struck the best balance of accuracy and simplicity. Later studies published by Geldart and Ling [28] and Cabrejos and Klinzing [29] lent further support to the validity of Rizk's

[27] equation under a wide range of experimental setups. While Hong and Tomita [30] developed a new correlation which slightly improved on Rizk's model, the group concluded that for dilute suspensions where the concentration of fluid outweighed the concentration of solid, Rizk's [27] equation performed better.

The mass flux and particle concentration profile development represent another area of saltation research with relevance to this thesis. Owen [31] hypothesized that the saltation layer would behave like aerodynamic roughness, and the concentration of particles in the layer would self-regulate based on the shear stress at the particle layer surface. He used these hypotheses to derive a set of equations describing the mass flux of particles in the saltation layer as well as the concentration of the particles. At the time, no data existed to directly verify the model for concentration, however Owen's work established a baseline for future researchers such as Nalpanis et al. [32] and Okoli [33]. Nalpanis et al. [32] simulated the concentration profile for 188 micron sand grains over a flat surface. While the simulation did not match experimental data near the threshold velocity (minimum velocity required to initiate saltation), as velocity increased, the simulation showed marked improvement in matching the experimentally measured concentration profile. Okoli's later study [33] improved upon Owen's [31] correlations for surface roughness. This study further supported Bagnold [23] and Owen's [31] hypothesis that the mass flux of particles in the saltation layer could not increase indefinitely with greater wind speeds, and instead an equilibrium condition exists.

The rate of re-entrainment of saltating particles back into a flow and its impact on the concentration profile within the flow is another area of saltation research with particular relevance to the present work. Researchers have shown that particles

undergoing saltating motion can resuspend back into the flow. For example, Nishimura and Hunt [34] conducted wind tunnel studies above a flat particle bed below a turbulent boundary layer and observed that as the wind speed increased, the particle trajectories became more erratic. While the geometry is admittedly different than the experiment this thesis is based upon, their hypothesis that when a particle was at the top of its saltation trajectory (i.e., with a vertical velocity of 0), turbulent eddies could disrupt the trajectory and keep the particle in suspension may still be applicable to the present work. Soldati and Marchioli [35] proposed a similar idea in a study which used Direct Numerical Simulation to model turbulent particle deposition and entrainment for a particle-laden channel flow. The study split the near wall region into three discrete layers and proposed that as particles entered the middle layer, turbulent structures could 'eject' the particles back out into the suspension.

## Research Gap

Researchers have extensively studied heat transfer in particle-laden flows [2,3,6,10–18] and the saltating motion of solid particles exposed to a flow [21–33], however little has been done to simultaneously study the two. Ultimately, Masters utilized the aforementioned Rizk [27] equation to choose gas velocities and particle concentrations which would keep particles entrained in the flow, however the modeling efforts of Hassan et al. [5] predicted significant particle settling, especially at the lowest Reynolds number tested of $3x10^4$. As there was no experimental way to verify if particles did in fact remain entrained or if some particles may have settled within the experiment of Ref. [6], this Thesis will work under the assumption that the settling predicted in Ref. [5] does occur. If particle settling did occur within the experiment of Ref. [6], the

literature suggests that a settled bed of particles exposed to a flow cannot be treated identically to the dispersed particle phase as the physics of heat transfer and drag are not identical. This observation, when taken into consideration with the discrepancies in Hassan et al.'s [5] CFD model, suggests that the impact of this particle layer is non-trivial and must be accounted for.

## Research Objective

The objective of this thesis is to improve the capability of Hassan et al.'s [5] previously developed Eulerian CFD model. To meet this goal, this thesis introduces new models for drag and heat transfer to properly account for the layer of settled particles in Masters' [6] experiment. Furthermore, models for the mass transfer between the dispersed particle phase and the settled particle phase are incorporated to account for particle impaction/sedimentation along with particle diffusion to the settled layer. These models were tested using the CFD code NPHASE [36] to evaluate whether the new models produce physical and/or improved results. Finally, suggestions for future models will be presented so that this work may act as a stepping stone to developing more robust models that can be used to predict the heat transfer performance of particle laden flows in a wide range of applications.

# Chapter 2 Theoretical Formulation

## 2.1 Governing Equations

### 2.1.1 Differential Models

As this thesis built on the modeling work of Hassan et al., the governing equations are extensions of those presented in Ref. [5]. The governing equations follow an Eulerian-Eulerian multiphase formulation where conservation of mass, momentum, and energy equations, which are written for compressible constituents in ensemble averaged form as follows:

$$\frac{\partial\left(\alpha^k\rho^k u_i^k\right)}{\partial x_i} = -\sum_{k\neq l}^{nf}\Gamma^{kl} + \sum_{k\neq l}^{nf}\Gamma^{lk} \tag{1}$$

$$\frac{\partial\left(\alpha^k\rho^k u_i^k u_j^k\right)}{\partial x_j} = -\alpha^k\frac{\partial p}{\partial x_j} + \alpha^k\rho^k g_i + \frac{\partial\tau_{ij}}{\partial x_j} + \sum_{k\neq l}^{nf} D^{kl}\left(u_i^l - u_i^k\right) + M_i^{kl} - \sum_{k\neq l}^{nf}\Gamma^{kl}\,u_i^k + \sum_{k\neq l}^{nf}\Gamma^{lk}\,u_i^l \tag{2}$$

$$\frac{\partial\left(\alpha^k\rho^k u_j^k h^k\right)}{\partial x_j} = \dot{q}_w^k + \frac{\partial}{\partial x_j}\left[\frac{\mu_t\alpha^k}{Pr_t}\frac{\partial h}{\partial x_j}\right] + \sum_{k\neq l}^{nf} Q^{kl}(T^l - T^k) - \sum_{k\neq l}^{nf}\Gamma^{kl}\,h_i^k + \sum_{k\neq l}^{nf}\Gamma^{lk}\,h_i^l \tag{3}$$

where,

$$\tau_{ij} = \mu_t\alpha^k\left[\left(\frac{\partial u_i^k}{\partial x_j} + \frac{\partial u_j^k}{\partial x_i}\right) - \frac{2}{3}\left(\frac{\partial u_i^k}{\partial x_i}\right)\delta_{ij}\right] - \frac{2}{3}\alpha^k\rho^k k^k\delta_{ij} \tag{4}$$

The above equations (1-4) were left in general form such that they can be applied to future work with more than the three fields at play in this thesis. The superscript *k*

refers to the *donor* phase and the superscript *l* refers to the *receptor* phase when inter-field interactions occur. The equations contain terms to account for the interfacial forces (drag and non-drag) as well as heat transfer, and mass transfer which were of particular interest in this thesis. Additionally, it must be noted that the momentum and energy equation forms above are Reynolds averaged (double averaging [37,38]), and eddy viscosity, $\mu_t$, is modeled. Accordingly, the time dependent and molecular diffusion terms are zero

The Coakley $q-\omega$ turbulence model [39] is used to model the turbulence in the gas phase only. The high Reynolds number form of the Coakley model is written without the phase indicator superscripts for the continuous gas phase (henceforth referred to as *k=0*) as follows:

$$\frac{\partial(\alpha\rho q u_j)}{\partial x_j} = \frac{\partial}{\partial x_j}\left[\frac{\mu_t \alpha}{\sigma_k}\frac{\partial q}{\partial x_j}\right] + \frac{\alpha P q}{2} - \frac{\alpha\rho\omega q}{2} \tag{5}$$

$$\frac{\partial(\alpha\rho\omega u_j)}{\partial x_j} = \frac{\partial}{\partial x_j}\left[\frac{\mu_t \alpha}{\sigma_\omega}\frac{\partial \omega}{\partial x_j}\right] + \frac{C_{\omega 1} C_\mu \rho 2 P q}{\mu_t} - C_{\omega 2}\alpha\rho\omega^2 \tag{6}$$

$$P = \tau_{ij}\frac{\partial u_i}{\partial x_j} \tag{7}$$

$$\mu_t = \rho C_\mu \frac{q^2}{\omega} \tag{8}$$

At the walls, standard wall function boundary conditions are used for the momentum, energy and turbulence equations [40] as shown below:

$$\tau_w = \frac{\alpha_P \rho_P C_\mu^{1/4} q_P |V|_P}{U^+} \tag{9}$$

$$T_w = \frac{1}{C_P}\left(\frac{q_w'' \alpha_P Pr_t U^+}{\rho C_\mu^{1/4} q_P}\right) + h_P \tag{10}$$

$$\frac{\alpha P q}{2} \rightarrow \left[\frac{C_{\mu}^{1/2}\alpha\rho q|V|}{2\Delta_w}\right]_P \tag{11}$$

$$\frac{\alpha\rho\omega q}{2} \rightarrow \left[\frac{C_{\mu}^{3/4}\alpha\rho q^2}{2U^+\Delta_w}\right]_P \tag{12}$$

$$\omega_P = \frac{C_{\mu}^{3/4} q}{\kappa\Delta_w} \tag{13}$$

where,

$$U^+ = \frac{1}{\kappa}\ln(Ey^+) \tag{14}$$

$$y^+ = \frac{\rho\Delta_w u_\tau}{\mu} \tag{15}$$

$$u_\tau \equiv \sqrt{\tau_w/\rho} \tag{16}$$

The turbulence modeling constants referenced above are $C_\mu = 0.09$, $\kappa = 0.42$, $E = 9.79$, $C_{\omega 1} = 1.0$, $C_{\omega 2} = 0.92$, $\sigma_q = 1.0$, $\sigma_\omega = 1.3$.

### 2.1.2 Physical Modeling

The work in Ref. [4] which this thesis extends utilized two different fields; a dispersed particle field, and a gas field. When modeling the behavior from the experiment in Ref. [5], the results had a reasonable match to the experimental data, however it was observed that particles were settling to the bottom of the flow channel. If particles settle along the bottom of the flow channel, it is no longer reasonable to treat them as a dispersed field, and it was hypothesized that properly accounting for the settled particles would improve the modeling of the experiment from Ref. [5]. For the present work, which is an extension of Ref. [5], three fields were considered; a gas phase (*k*=0), a

dispersed solid phase ($k$=1), and a settled particle phase which will be referred to as a particle film throughout this thesis ($k$=2). Accordingly, models for the drag and heat transfer between dispersed particle and gas are presented below. Separate models are presented for the shear dominated drag between the particle film and the gas and the heat transfer between the film and the gas. Finally mass transfer models to account for the settling of dispersed particles along with the re-entrainment of particles from film back to dispersed solid are presented. Heat transfer and drag between the dispersed particles ($k$=1) and particle film ($k$=2) are neglected in the present work, since the volume fraction of particles remains quite low in the core flow.

For the dispersed particles, the Schiller and Neuman [20] smooth spherical particle model is used:

$$\mathrm{D}^{kl} = \frac{3}{4}\frac{\mathrm{C_D}\alpha^0\alpha^l\rho^0}{\mathrm{d}^{p,l}}\left|\mathrm{u}_\mathrm{i}^l - \mathrm{u}_\mathrm{i}^k\right| \tag{17}$$

$$\mathrm{C_D} = \frac{24(1+.15[\mathrm{Re}^{p,l}]^{.687})}{\mathrm{Re}^{p,l}} \tag{18}$$

The particle Reynolds number in equation 18 is defined:

$$\mathrm{Re}^{p,l} \equiv \frac{\rho^0\left|\mathrm{u}_\mathrm{i}^l - \mathrm{u}_\mathrm{i}^k\right|\mathrm{d}^{p,l}}{\mu^0} \tag{19}$$

where $\mathrm{u}_\mathrm{i}^l - \mathrm{u}_\mathrm{i}^k$ is the local relative velocity between the dispersed particle field $l$ and continuous gas field $k=0$, and $\mathrm{d}^{p,l}$ is the field $l$ particle diameter. All particle field Reynolds numbers tested in this thesis do not exceed 500 and therefore fall within the applicable range of equation 18. Turbulence dispersion at the gas and particle interfaces was accounted for per Lopez de Bertodano [21]:

$$M_i^{0l} = C_{TD}\rho^0 k^0 \frac{\partial \alpha^l}{\partial x_i} \quad (20)$$

Properly modeling the drag between the particle layer and the gas was accomplished by adapting a conventional wall friction for a moving wall. In this way the surface of the layer is treated as a no slip moving wall. The sketch of a cell adjacent to the wall is presented below.

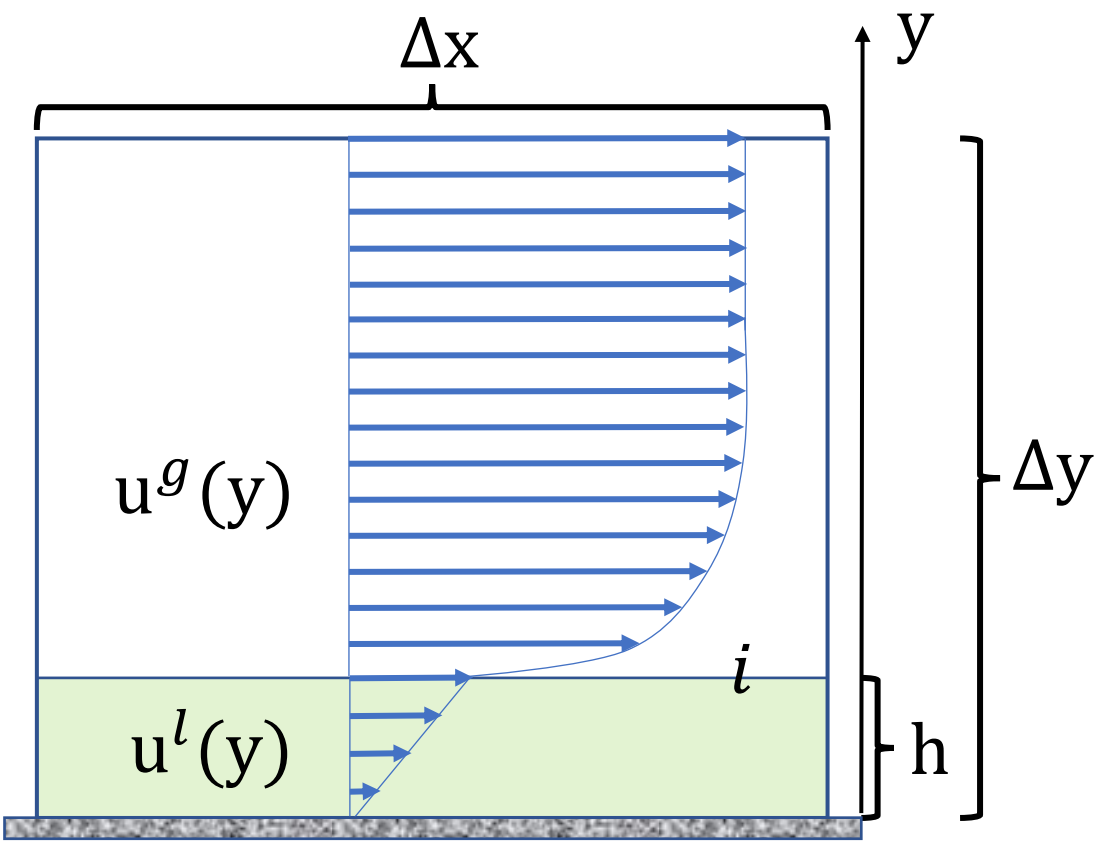


***Figure 1:*** *Velocity profiles of a wall adjacent cell. $u^l$ refers to the particle layer velocity and $u^g$ refers to the gas velocity.*

Since the layer thickness and velocity are small, a Couette/linear velocity profile is chosen. The velocity and shear stress are continuous at the interface *i*:

$$u^l(h) = u^g(h) \quad (21)$$

$$\tau^{l}(\mathrm{h}) = \tau^{g}(\mathrm{h}) \rightarrow \mu^{l} \left.\frac{\mathrm{du}^{l}}{\mathrm{dy}}\right|_{\mathrm{y=h}} = \mu_{\mathrm{t}}^{g} \left.\frac{\mathrm{du}^{g}}{\mathrm{dy}}\right|_{\mathrm{y=h}} \tag{22}$$

Superscripts refer to the phase (*g* for gas and *l* for particle layer). The turbulent viscosity in the gas core is taken as $\mu_{\mathrm{t}}^{g}$, which is obtained from equation 8. Layer thickness *h* is a function of the volume fraction with the assumption that all of the deposited particles form a flowing constant thickness layer along the wall.

$$\mathrm{h} = \frac{\alpha^{l} \forall}{\mathrm{A}} \tag{23}$$

where ∀ refers to the cell volume and A is the cells cross sectional area. For figure 1 above $\mathrm{A} = \Delta\mathrm{x}\Delta\mathrm{y}$, $\forall = \Delta\mathrm{x}\Delta\mathrm{y}\Delta\mathrm{z}$ (z into page).

The interface velocity, $\mathrm{u}^{i}$, is computed by evaluating the shear force exerted on each phase there per the following.

$$\tau^{k} = \mathrm{T}^{k}(\mathrm{u}_{\mathrm{P}}^{k} - \mathrm{u}_{\mathrm{w}}^{k}) \tag{24}$$

Here, superscript *k* applies to both liquid and gas phases. $\mathrm{u}_{\mathrm{P}}^{k}$ is the cell average of the axial velocity, and $\mathrm{u}_{\mathrm{w}}^{k}$ is the nominal wall velocity. The no slip condition is applied therefore $\mathrm{u}_{\mathrm{w}}^{l} = 0$. $\mathrm{u}_{\mathrm{w}}^{g} = \mathrm{u}^{i}$ which is the boundary velocity of interest. The $\mathrm{T}^{k}$ term is the phase and turbulence model dependent shear-per-unit velocity term. For the particle layer $\mathrm{u}_{\mathrm{P}}^{l} = \mathrm{u}^{i}/2$ therefore $\mathrm{T}^{l} = \frac{\mu^{l}}{\mathrm{h}/2}$. For the gas core flow $\tau^{g} = \mathrm{T}^{g}(\mathrm{u}_{\mathrm{P}}^{g} - \mathrm{u}^{i})$ and as the flow is turbulent $\mathrm{T}^{g}$ is a turbulent model dependent function of the transport turbulence variables.

The interfacial drag is conformed to the terms $\mathrm{D}^{gl}\left(\mathrm{u}_{\mathrm{i}}^{l} - \mathrm{u}_{\mathrm{i}}^{g}\right)$ that appear in the momentum equation (written more generically as $\mathrm{D}^{kl}\left(\mathrm{u}_{\mathrm{i}}^{l} - \mathrm{u}_{\mathrm{i}}^{k}\right)$). We note that $\mathrm{D}^{gl} = \mathrm{D}^{lg} =$

D, i.e., the drag force exerted by the phases on one another are equal in magnitude. Equation 24 as applied to the particle layer, $\tau^l = \mathrm{T}^l(\mathrm{u}_\mathrm{P}^l - \mathrm{u}_\mathrm{w}^l)$, can be written $\tau^l = \mathrm{T}^l(\mathrm{u}^i - \mathrm{u}_\mathrm{P}^l)$ due to the Couette flow assumption, where again $\mathrm{T}^l = \frac{\mu^l}{\mathrm{h}/2}$. So for particle layer and gas we have at the particle layer-gas core interface

$$\tau^l \mathrm{A} = \tau^g \mathrm{A} \tag{25}$$

Substituting equation 24 into equation 25 yields:

$$\mathrm{T}^l\left(\mathrm{u}^i - \mathrm{u}_\mathrm{P}^l\right)\mathrm{A} = \mathrm{T}^g(\mathrm{u}_\mathrm{P}^g - \mathrm{u}^i)\mathrm{A} \tag{26}$$

Which can be solved for the interfacial velocity

$$\mathrm{u}^i = \frac{\mathrm{T}^g \mathrm{u}_\mathrm{P}^g + \mathrm{T}^l \mathrm{u}_\mathrm{P}^l}{\mathrm{T}^g + \mathrm{T}^l} \tag{27}$$

Substituting equation 27 into equation 26 we obtain the drag force exerted on the particle layer and gas core respectively

$$\mathrm{D}\left(\mathrm{u}_\mathrm{i}^g - \mathrm{u}_\mathrm{i}^l\right), \mathrm{D}\left(\mathrm{u}_\mathrm{i}^l - \mathrm{u}_\mathrm{i}^g\right) \tag{28}$$

where

$$\mathrm{D} = \frac{\mathrm{T}^l \mathrm{T}^g}{\mathrm{T}^g + \mathrm{T}^l}\mathrm{A} \tag{29}$$

In order to predict the overall pipe heat transfer and flow temperature distribution at play in the highly mass loaded copper powder system of interest in this thesis heat transfer models needed to be adopted. Heat transfer directly to the dispersed particle phase was neglected as the volume fractions encountered in the present work do not exceed 0.05, even at the maximum solids loading of 1.0. Heat transfer is instead partitioned to the

particle film phase and the gas phase, and interfacial heat transfer between the dispersed particle phase and the gas was modeled following the Ranz-Marshall correlation [41]:

$$Q^{kl} = \frac{6\lambda^0\alpha^0\alpha^l \mathrm{Nu}^{p,l}}{d^{p,l^2}} \tag{30}$$

$$\mathrm{Nu}^{p,l} = 2 + 0.6\mathrm{Re}^{p,l^{0.5}}\mathrm{Pr}^{0.3} \tag{31}$$

The thin film interfacial heat transfer model is an adaptation of conventional conjugate heat transfer, i.e., the surface of the film is treated as would a solid boundary between flow and conducting solid. The treatment for specified wall temperature vs. specified wall heat flux differ somewhat. Here we focus on the specified wall heat flux condition. It is applied similarly for both liquid films and particle layers – we assume a liquid film here. Consider a sketch of a cell, P, adjacent to the wall:

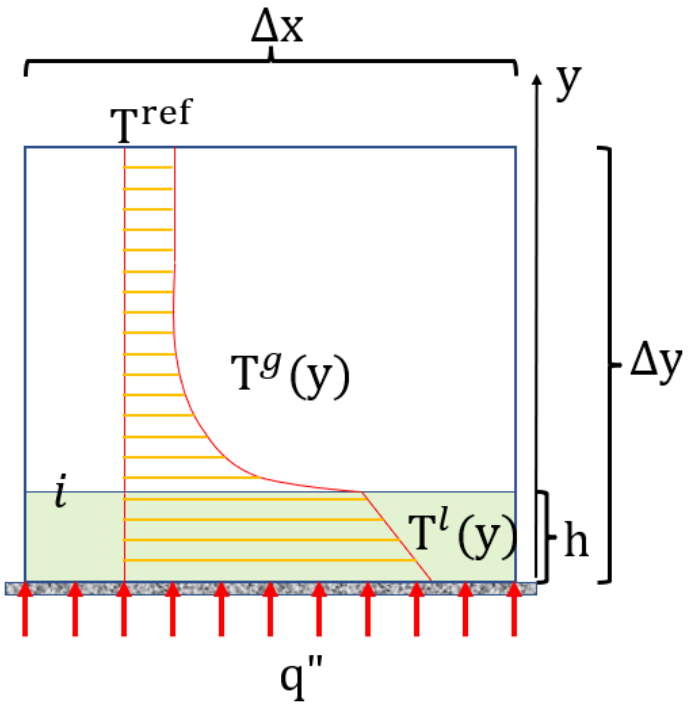


***Figure 2:*** *Temperature profile of a wall adjacent cell. $T^l$ refers to the film layer temperature and $T^g$ refers to the gas temperature profile.*

Film thicknesses and velocities are small, so a Couette/linear liquid velocity profile is adopted, per the thin-film drag model discussed above. Accordingly, the temperature profile within the film varies linearly. The gas flow will have a temperature profile appropriate for the flow regime (laminar, turbulent). The temperature is continuous at the interface, $i$:

$$\mathrm{T}^{i} = \mathrm{T}^{l}(\mathrm{h}) = \mathrm{T}^{g}(\mathrm{h}) \tag{32}$$

The vertical heat flux out of the film and into the gas are equivalenced at the interface. Referring to figure 2, taking positive wall flux into the wall as shown, we have for the film phase:

$$\mathrm{q}^{\prime\prime,\mathrm{int}} = -\mathrm{k}^{l}\left(\frac{\mathrm{T}^{i}-\mathrm{T}_{\mathrm{w}}}{\mathrm{h}}\right) \tag{33}$$

Superscripts $l$ represents the liquid phase, $\mathrm{k}^{l}$ is the thermal conductivity of the liquid. The linearity of the film temperature allows us to write equation (33) as

$$\mathrm{q}^{\prime\prime,\mathrm{int}} = -\mathrm{k}^{l}\left(\frac{\mathrm{T}^{i}-\mathrm{T}_{\mathrm{P}}^{l}}{\frac{\mathrm{h}}{2}}\right) = \mathrm{H}^{l}(\mathrm{T}^{i} - \mathrm{T}_{\mathrm{P}}^{l}) \tag{34}$$

where $\mathrm{T}_{\mathrm{P}}^{l}$ is the average film temperature, and $\mathrm{H}^{l} \equiv \frac{\mathrm{k}^{l}}{h/2}$, which can be viewed as a local film heat transfer coefficient. For the gas phase:

$$\mathrm{q}^{\prime\prime,\mathrm{int}} = \mathrm{H}^{g}(\mathrm{T}_{\mathrm{P}}^{g} - \mathrm{T}^{i}) \tag{35}$$

where $\mathrm{T}_{\mathrm{P}}^{g}$ is the average gas temperature, and $\mathrm{H}^{g}$ is a turbulence model dependent function of the transport turbulence variables. Equations (34) and (35) can be solved simultaneously for the interface temperature:

$$\mathrm{T}^{i} = \frac{\mathrm{H}^{g}\mathrm{T}_{\mathrm{P}}^{g}+\mathrm{H}^{l}\mathrm{T}_{\mathrm{P}}^{l}}{(\mathrm{H}^{l}+\mathrm{H}^{g})} \tag{36}$$

Once we have evaluated $h = \frac{\alpha^l \forall}{A}$ and $T^i$ from equation (32), using values of $T_P^g$ and $T_P^l$ from the previous iteration, we can implement the interfacial heating in the source terms of the energy equation.

Similar to the treatment of drag, the interfacial heat flux is conformed to the terms $Q^{gl}(T^l - T^g)$ that appear in the energy equation, and added implicitly to the energy equation in these functions (written more generically as $Q^{kl}(T^l - T^k)$). Specifically, the interfacial heat transfer directed from the liquid to the gas, $q''^{,\text{int}} = Q^{lg}(T^l - T^g)$. This term is added to the gas energy equation, and the equal and opposite term $Q^{gl}(T^g - T^l)$ is added to the film energy equation. Note that as with drag, $Q^{lg} = Q^{gl} = Q$. With equation (35) we set $q''^{,\text{int}} = Q(T^l - T^g) = H^g(T_P^g - T^i)$. With equation (36) we obtain:

$$Q = \frac{H^g H^l}{(H^l + H^g)} \tag{37}$$

Note that in order to treat these terms implicitly when our dependent transport variable is enthalpy rather than temperature, we need to introduce the specific heat of each phase:

$$Q(T^l - T^g) = \frac{Q}{C_P^g}\left(h^l \frac{C_P^g}{C_P^l} - h^g\right) = \frac{Q}{C_P^g}(h^l - h^g) + \frac{Q}{C_P^g} h^l \left(1 - \frac{C_P^g}{C_P^l}\right) \tag{38}$$

The terms in the orange are treated implicitly, since they are linear in the enthalpies. The terms in blue are added as conventional explicit and implicit source terms in the interfacial heat transfer functions.

The Nitrogen gas phase is treated as calorically perfect, and the specific heat is taken as constant for the pressure and temperature range at play in this thesis per [42] ($p_{sys}$ = 1.73 MPa, 290 K < T < 450 K). For $N_2$, we take $C_P$ = 1060 J/kg K, with a specific heat ratio and gas constant $\gamma$ = 1.388, R = 296.8 J/kg K. The Prandtl number was fixed at

Pr = 0.73 [43], and the dynamic viscosity was modeled using a power law fit to date obtained from [42] as the value varies significantly across the temperature range at play. This fit is shown below:

$$\mu^{N_2}\left(\frac{kg}{m\,s}\right) = 2.94x10^{-7}T^{.723}, p_{sys} = 1.73MPa,\ 295K < T < 475K \quad (39)$$

For the copper powder, the phasic density and heat capacity was taken as 8960 kg/m$^3$ and 385 J/kg K respectively.

At the entrance of the flow channel all of the solid phase is found in the dispersed field, with no particle film layer present. However, by virtue of the impaction/sedimentation and diffusion of the particle phase, there is a subsequent buildup of a particle layer along the bottom of the flow channel. As the heat transfer and drag behavior of the dispersed particles and the particle film layer is different, it was important to model this mass transfer. Refer to figure 3 below for a visual when referencing this mass transfer model.

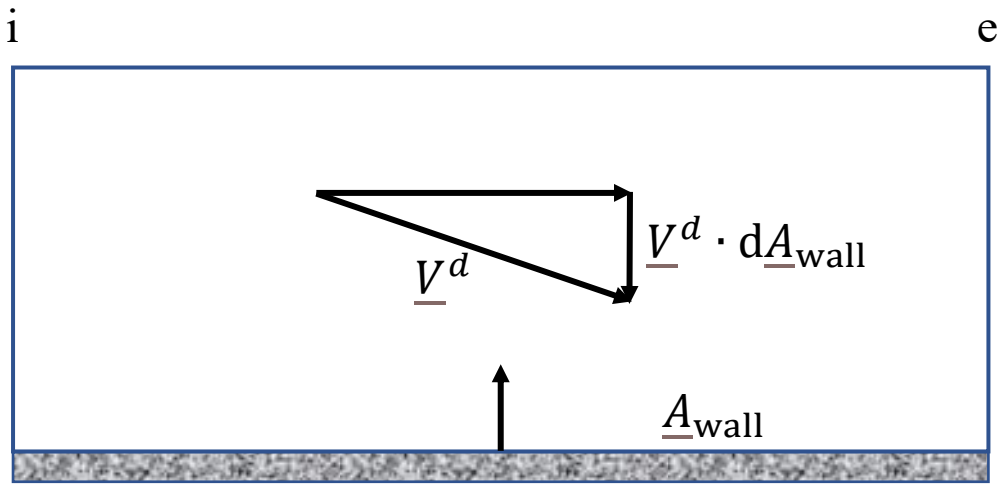


***Figure 3**: Velocities vectors for inter-field mass transfer from dispersed particle to particle film.*

The mass transfer rate from impaction/sedimentation was designated as $\Gamma_{\mathrm{conv}}^{d-c}$. The subscript refers to the convection normal to the wall or existing film which causes the disperse particle phase to the be donated to the film layer. $\Gamma_{\mathrm{conv}}^{d-c}$ is calculated per the following:

$$\Gamma_{\mathrm{conv}}^{d-c} = \left\| \int_{\mathrm{wall}} \rho^{d} \alpha^{d} \left( \underline{\mathrm{V}}^{d} \cdot \mathrm{dA}_{\mathrm{wall}} \right), 0 \right\| \tag{40}$$

Superscript *d* and *c* refers to the disperse and continuous fields respectively and *d-c* designates the disperse-continuos donor-receptor mass transfer. Equation (40) states that the dispersed field convective deposition rate is equal to the cell mass flux directed at the wall and has units of mass/time.

Beyond convective deposition from impaction/sedimentation, dispersed particles may transfer to the continuous particle film phase through diffusion. When the mean disperse field velocity runs parallel to the wall, there can be deposition due to Brownian motion (laminar diffusion) or turbulent fluctuations of the continuous field normal to the wall (turbulent diffusion). We employ a standard gradient diffusion approximation that adapts from a conventional wall-function approach for the turbulence model used.

$$\Gamma_{\mathrm{diff}}^{d-c} = \int_{\mathrm{wall}} \mathrm{J}^{d} \mathrm{dA}_{\mathrm{wall}}, \mathrm{J}^{d} = \frac{\mathrm{K} \rho^{d} \alpha^{d} \mathrm{u}_{\tau}^{c}}{\mathrm{Sc}_{\mathrm{t}} \, \mathrm{u}^{c+}} \tag{41}$$

In equation (41), $\mathrm{u}_{\tau}^{c}$ is the continuous field friction velocity, $\mathrm{Sc}_{\mathrm{t}}$ is the turbulent Schmidt number (taken as 1 here), $\mathrm{u}^{c+}$ is the non-dimensional log-layer velocity ($\mathrm{u}^{c+} = \frac{1}{\kappa} \ln (E y^{+}) =$ here), and K is a calibration constant that can be varied for the class of flows considered per validation against experimental data.

Taken together the mass transfer from dispersed particle phase to continuous particle film phase can be expressed as:

$$\Gamma^{d-c} = \Gamma^{d-c}_{\text{conv}} + \Gamma^{d-c}_{\text{diff}} = \left\| \int_{\text{wall}} \rho^d \alpha^d \left( \underline{V}^d \cdot \mathrm{dA}_{\text{wall}} \right), 0 \right\| + \int_{\text{wall}} J^d \mathrm{dA}_{\text{wall}}, J^d = \frac{K \rho^d \alpha^d u_t^c}{Sc_t \, u^{c+}} \quad (42)$$

The re-entrainment of particles back into the field is a complex process which here is modelled as "fully developed" saltation, i.e., a) the shear stress exerted on the layer by the core flow is well beyond the inception shear stress where particles just begin to bounce and move, and b) the shear-induced uptake mass flux is much larger than that due to splashing, bouncing, and re-depositing of particles. Accordingly, these physics are neglected, and the mass flux is modeled following Creyssels et al. [44]:

$$\Gamma^{l-d} = \rho^p d^p \sqrt{g d^p} X (S^* - S_c) \frac{\forall}{A_{\text{wall}}} \quad (43)$$

where $S^*$ is the Shields number.

$$S^* = \frac{\tau_w}{[(\rho^p - \rho^c) g d^p]} \quad (44)$$

In equation 43, $S_c$ is the critical Shields number below which no saltation can occur, $S_c \cong 0.01$., and $X$ is an empirical constant, $X \cong 28$. We note that the "wall" shear stress used in equation (44), is the particle layer interfacial stress computed per equation (24) above.

## 2.2 Numerics

### 2.2.1 Baseline Numerics

The new models were implemented and tested using the CFD code NPHASE [36]. NPHASE works under the principles of well-established second order finite volume discretization practices and a segregated pressure-correction based solution strategy. In

order to better understand the workings of NPHASE, a simplified theory manual for the Eulerian Multiphase flow modeling is presented below. This simplified model will consider a 1-D, axially oriented, inviscid flow, with simple 1st order upwind discretization. Algorithmic elements including multiphase flow an drag treatment are accommodated in this simplified model in sections 2.2.2 and 2.2.3 respectively.

Simply put, the NPHASE algorithm considers the momentum equation and continuity for each field present. By default, NPHASE solves a mixture continuity equation and all of the field continuity equations (i.e. volume fraction equations). This means that continuity is over-specified and an additional "Carver" volume fraction normalization step to ensure that the volume fraction sum to 1 (realizability) [45]. This is beyond the scope of what is treated here so we start simply with the momentum and volume fraction.

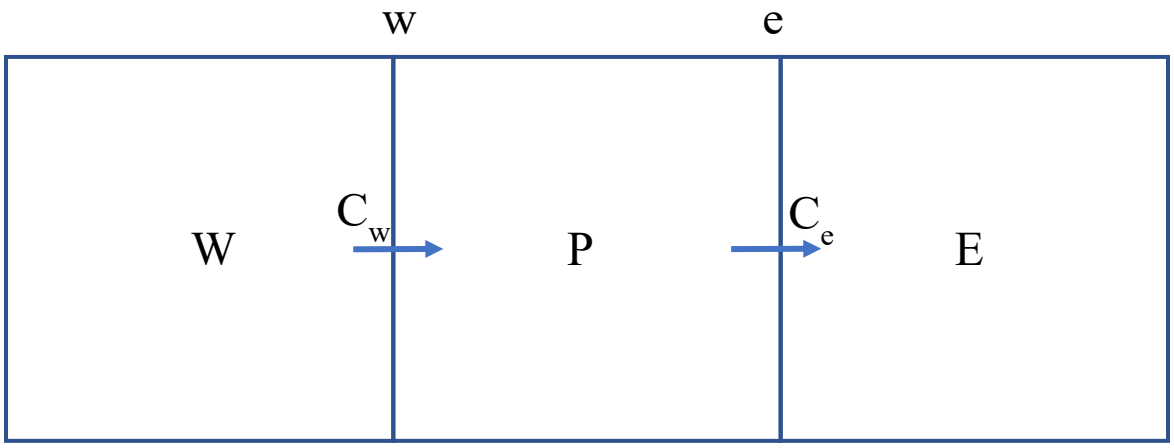


***Figure 4**: 1-D axially oriented discretization model*

Per the figure above, consider 1D momentum equation, 1-field, inviscid discretization using 1st order upwind, with velocity in the +x direction:

$$C_e u_P^{n+1} = C_w u_W^{n+1} + SU \tag{45}$$

where $C_{face} \equiv (\rho \alpha u A)_{face}$ and SU in this case contains only the pressure gradient.

The way this is implemented in the code is as follows:

$$(A_P + \|C, 0\|)u_P^{n+1} = A_w u_W^{n+1} + SU + (\|C, 0\| - C)u_P^n \quad (46)$$

where $C \equiv C_e - C_w$, and where $A_W = C_w$ and $A_P$ is evaluated per:

$$A_P = \sum_{i=1}^{nface} A_i \quad (47)$$

so here we have $A_P = C_w$.

The C's within equation 46 are added to ensure *diagonal domina*nce of the discrete system of equations so we can use simple iterative solution strategies to solve them. There are 2 cases to explore why the C's appear as they do in (46).

Case 1, C > 0:

For $C > 0$, substituting for C yields: $C_e - C_w > 0$ which implies $C_e > C_w$

Which gives: $\|C, 0\| = C, \|C, 0\| - C = 0$ from within equation 46.

So (46) becomes

$$C_e u_P^{n+1} = C_w u_W^{n+1} + SU \quad (48)$$

In exact agreement with (45), i.e., nothing happens for the case where $C_e - C_w > 0$, since for a C > 0, equation (46) is already diagonally dominant.

Case 2, C < 0:

As $C < 0$, substituting for C yields: $C_e - C_w < 0$ which implies that $C_e < C_w$

Which gives: $\|C, 0\| = 0, \|C, 0\| - C = -C$ from within equation 46.

So (46) becomes

$$C_w u_P^{n+1} = C_w u_W^{n+1} + SU - (C_e - C_w)u_P^n \quad (49)$$

This expression is neutrally diagonally dominant. At convergence, $u_P^{n+1} = u_P^n$, and therefore we are left with $C_e u_P = C_w u_W + SU$ consistent again with (45). To summarize, the code implements a relaxation factor due to mass imbalance of the precise size needed (if needed, i.e., if C < 0) to render the matrix system to be solved neutrally diagonally dominant. Since $C \to 0$ at convergence both $\|C, 0\|$ and $(\|C, 0\| - C)$ become zero as well.

### 2.2.2 Multiphase Flow

Next up we will discuss adding multiphase flow capability. Starting with the no mass transfer case. For phasic momentum the above discussion applies, i.e., our discrete scalar equation for field *k* is:

$$\left(A_P^k + \|C^k, 0\|\right)u_P^{k,n+1} = A_w u_W^{k,n+1} + SU^k + (\|C^k, 0\| - C^k)u_P^{k,n} \quad (50)$$

Which again guarantees diagonal dominance and returns $C_e^k u_P^k = C_w^k u_W^k + SU^k$ at convergence, where $C_{face}^k \equiv (\rho^k \alpha^k u^k A)_{face}$, and again SU contains only the pressure gradient.

For the volume fraction equation things are a bit different since $\alpha$ is part of the flux itself.

Once again 1D, using 1st order upwind, with velocity in the +x direction, the volume fraction equation becomes:

$$€_e^k \alpha_P^{k,n+1} = €_e^k \alpha_W^{k,n+1} + SU \quad (51)$$

where $€_{face}^k \equiv (\rho^k u^k A)_{face}$, and SU here is zero unless there is mass transfer.

Now we proceed as we do above:

$$\left(\mathrm{A}_{\mathrm{P}}^{k}+\|€^{k},0\|\right)\alpha_{\mathrm{P}}^{k,\mathrm{n}+1}=\mathrm{A}_{\mathrm{w}}\alpha_{\mathrm{W}}^{k,\mathrm{n}+1}+\mathrm{SU}^{k}+(\|€^{k},0\|-€^{k})\alpha_{\mathrm{P}}^{k,\mathrm{n}} \tag{52}$$

In the case with $€^{k}\equiv €_{e}^{k}-€_{w}^{k}$, $€^{k}>0$ yields

$$€_{\mathrm{e}}^{k}\alpha_{\mathrm{P}}^{k,\mathrm{n}+1}=€_{\mathrm{w}}^{k}\alpha_{\mathrm{W}}^{k,\mathrm{n}+1}+\mathrm{SU} \tag{53}$$

as before, but in the case $€^{\mathrm{k}}<0$, equation (52) yields:

$$€_{\mathrm{w}}^{k}\alpha_{\mathrm{P}}^{\mathrm{n}+1}=€_{\mathrm{w}}^{k}\alpha_{\mathrm{W}}^{\mathrm{n}+1}+\mathrm{SU}^{k}-(€_{\mathrm{e}}^{k}-€_{\mathrm{w}}^{k})\alpha_{\mathrm{P}}^{\mathrm{n}} \tag{54}$$

Once again at convergence we have

$$€_{\mathrm{e}}^{k}\alpha_{\mathrm{P}}^{k}=€_{\mathrm{w}}^{k}\alpha_{\mathrm{W}}^{k}+\mathrm{SU} \tag{55}$$

The only difference is that $€^{k}\ \mathrm{does\ not}\rightarrow 0$ so at convergence one of the terms $\|€^{k},0\|$ or $(\|€^{k},0\|-€^{k})$ does *not* go to zero.

Now we consider the effect of mass transfer. Starting with a modification of the volume fraction equation (Equation (50)):

$$\left(\mathrm{A}_{\mathrm{P}}^{k}+\left\|€^{k},0\right\|\right)\alpha_{\mathrm{P}}^{k,\mathrm{n}+1}=\mathrm{A}_{\mathrm{w}}\alpha_{\mathrm{W}}^{k,\mathrm{n}+1}+\mathrm{SU}^{k}+\left(\left\|€^{k},0\right\|-€^{k}\right)\alpha_{\mathrm{P}}^{k,\mathrm{n}}-\Gamma^{kl}\alpha_{\mathrm{P}}^{k,\mathrm{n}+1}+\Gamma^{lk}\alpha_{\mathrm{P}}^{l,\mathrm{n}+1} \tag{56}$$

Terms $k$ and $l$ in the red mass transfer terms represent donor and receptor fields. $\Gamma^{kl}$ is the donor mass transfer kernel. $\Gamma^{lk}$ is the receptor mass transfer kernel. Notice that the terms from Equation (51) themselves do not include mass transfer, i.e., $€^{k}\equiv €_{e}^{k}-€_{w}^{k}$.

To see how mass transfer is implemented we need to consider the *Δ-form* of the discretized equations that are used in the code. Embedding equation 46 terms into the source terms with an overbar, (46) becomes:

$$\overline{\mathrm{A}}_{\mathrm{P}}^{k}\alpha_{\mathrm{P}}^{k,\mathrm{n}+1} = \mathrm{A}_{\mathrm{W}}^{\mathrm{k}}\alpha_{\mathrm{W}}^{k,\mathrm{n}+1} + \overline{\mathrm{SU}}^{k} - \Gamma^{kl}\alpha_{\mathrm{P}}^{k,\mathrm{n}+1} + \Gamma^{lk}\alpha_{\mathrm{P}}^{l,\mathrm{n}+1} \quad (57)$$

where:

$$\overline{\mathrm{A}}_{\mathrm{P}}^{k} \equiv \left(\mathrm{A}_{\mathrm{P}}^{k} + \|\mathrm{C}^{k}, 0\|\right), \overline{\mathrm{SU}}^{k} \equiv \mathrm{SU}^{k} + (\|€^{k}, 0\| - €^{k})\alpha_{\mathrm{P}}^{k,\mathrm{n}} \quad (58)$$

To convert to Δ-form we subtract $\overline{\mathrm{A}}_{\mathrm{P}}^{k}\alpha_{\mathrm{P}}^{k,\mathrm{n}}$ from the RHS and LHS, and add $\left(\mathrm{A}_{\mathrm{W}}\alpha_{\mathrm{W}}^{k,\mathrm{n}} - \mathrm{A}_{\mathrm{W}}\alpha_{\mathrm{W}}^{k,\mathrm{n}} + \Gamma^{kl}\alpha_{\mathrm{P}}^{k,\mathrm{n}} - \Gamma^{kl}\alpha_{\mathrm{P}}^{k,\mathrm{n}} - \Gamma^{lk}\alpha_{\mathrm{P}}^{l,\mathrm{n}} + \Gamma^{lk}\alpha_{\mathrm{P}}^{l,\mathrm{n}}\right)$, which ≡ 0, to the RHS.

This yields:

$$\overline{\mathrm{A}}_{\mathrm{P}}^{k}\Delta\alpha_{\mathrm{P}}^{k} = \mathrm{A}_{\mathrm{W}}\Delta\alpha_{\mathrm{W}}^{k} + \overline{\mathrm{SU}}^{k} - \Gamma^{kl}\Delta\alpha_{\mathrm{P}}^{k} + \Delta\Gamma^{lk}\alpha_{\mathrm{P}}^{l} + \left(-\overline{\mathrm{A}}_{\mathrm{P}}^{k}\alpha_{\mathrm{P}}^{k,\mathrm{n}} + \mathrm{A}_{\mathrm{W}}\alpha_{\mathrm{W}}^{k,\mathrm{n}} - \Gamma^{kl}\alpha_{\mathrm{P}}^{k,\mathrm{n}} + \Gamma^{lk}\alpha_{\mathrm{P}}^{l,\mathrm{n}}\right) \quad (59)$$

The terms in red are added to the explicit source term, $\overline{\mathrm{SU}}^{k}$. So designating this new explicit source term as $\overline{\overline{\mathrm{SU}}}^{k}$, our discrete equations become:

$$\overline{\mathrm{A}}_{\mathrm{P}}^{k}\Delta\alpha_{\mathrm{P}}^{k} = \mathrm{A}_{\mathrm{W}}\Delta\alpha_{\mathrm{W}}^{k} + \overline{\overline{\mathrm{SU}}}^{k} - \Gamma^{kl}\Delta\alpha_{\mathrm{P}}^{k} + \Delta\Gamma^{lk}\alpha_{\mathrm{P}}^{l} \quad (60)$$

(16) is the discrete equation for volume fraction correction. Once this system has been solved for each field, the new volume fractions are updated:

$$\alpha_{\mathrm{P}}^{k,n+1} = \alpha_{\mathrm{P}}^{k,n} + \Delta\alpha_{\mathrm{P}}^{k} \quad (61)$$

### 2.2.3 Continuous-Particle Layer Drag Treatment

NPHASE implements the drag model discussed in 2.1.2 as follows. For the film, the velocity is set to:

$$\mathrm{u}_{\mathrm{P}}^{l} = \mathrm{u}^{i}/2 \quad (62)$$

where $u^i$ is evaluated from equation (27). Equation (62) is enforced by setting the implicit and explicit source terms, SP and SU:

$$SU = -10^{20} \tag{63}$$

$$SU = 10^{20} * u^i/2 \tag{64}$$

where $10^{20}$ is chosen to be a machine large number within NPHASE. This renders negligible all other terms in the discrete governing equation for the film phase which now reads:

$$10^{20} * u_P^{l,n+1} = 10^{20} * \frac{u^i}{2} \rightarrow u_P^{l,n+1} = \frac{u^i}{2} \tag{65}$$

For the gas phase, all of the other transport terms are present so with $\tau^g = T^g(u_P^g - u_w^g)$, the implicit and explicit source terms become (shear is added as a force applied to volume of gas occupying the cell)

$$SP = -T^g \alpha^g A^i \tag{66}$$

$$SU = T^g \alpha^g A^i u^i \tag{67}$$

where $A^i$ is the interface area which is equal to the wall area in our model ($A^i = \Delta x \Delta z$ here) since the film is thin.

# Chapter 3 Results and Discussion

## 3.1 Experimental Setup

Masters' experimental setup [6] which forms the basis for this thesis is shown below in figure 5. Masters utilized a pressure regulator and mass flow controller to control the Reynolds number of the Nitrogen carrier gas. This Nitrogen gas was able to bypass the powder feed system when gas only cases were desired, or could be directed through the powder feed system to add copper powder to the specified solid loading utilizing an auger particle injection system. The combined flow equalized in the entry length tubing and then entered the heated test section. The test section was wrapped with heat tape to achieve a uniform heat flux. After exiting the test section, the flow entered a filter which recovered the solid particles. The weight of the recovered particles along with the total time of the test yielded the experimental mass flow rate which was used to fine tune the rate of particle injection to the specified solid loading. The final component in the experimental setup was a backpressure regulator which maintained the backpressure for the heated test section to approximately 17 bar.

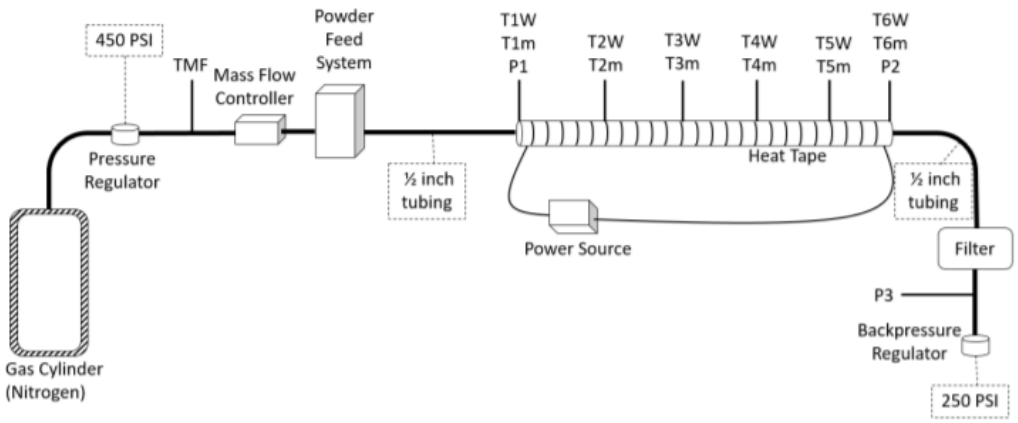


***Figure 5****: Schematic of Masters experimental setup. [5]*

Within the heated test section, thermocouples measured the temperature of the flow at six axial locations. At each of the six locations, one thermocouple was placed between 0.003587m and 0.004400 m above the centerline of the pipe to measure the flow temperature, and a second thermocouple was welded to the outside of the pipe to monitor wall temperatures. A typical test case would involve waiting for steady state to be achieved, and then recording thermocouple readings at each location for 30 seconds. The average value recorded was taken as the temperature value for each case. The thermocouples used had a special limit error of $\pm$.4% or 1.1 k (whichever is greater) and this was utilized as the bias error for all flow readings. [6]

Masters' experimental results will not be a focus for this thesis, but this experimental setup was the motivation for the CFD work of Hassan et al. [4] which this thesis will build upon. Hassan et al. [4] discretized the test chamber into a cylindrical mesh comprised of 12264 hexahedral cells as pictured in Figures 6 and 7.

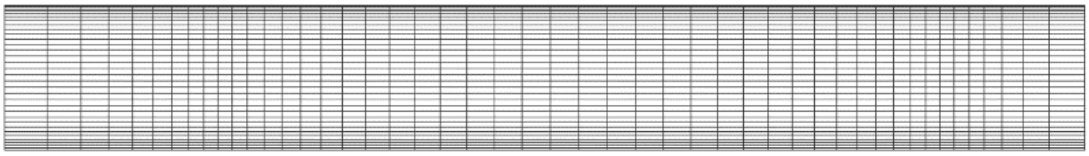

***Figure 6**: Axial distribution of points from Hassan et al. [4]*

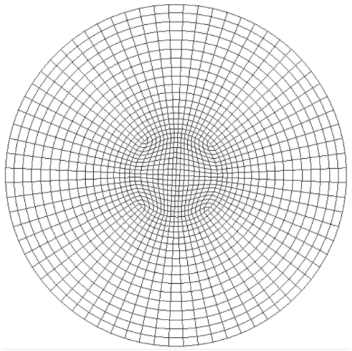

***Figure 7**: Cross section of computational mesh from Hassan et al. [4]*

The group found that as solids loading went up, wall temperature decreased indicative of the higher thermal mass. This phenomenon can be seen below in figure 8.

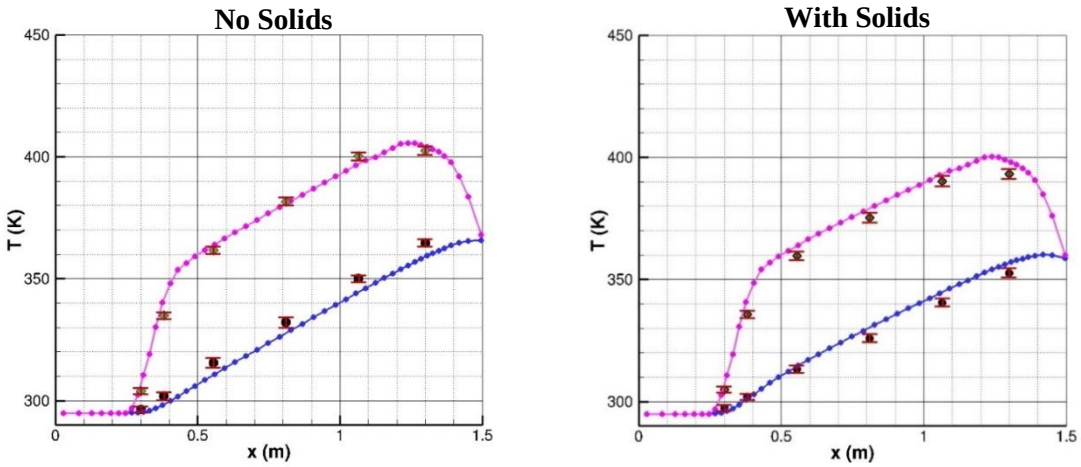


***Figure 8:** Wall temperature vs axial position in pink. Flow temperature vs axial position in blue. Black dots with error bars represent Masters' experimental results with error bars. Notice that wall temperature is lower with solids added. [4]*

However, as can be seen below in figure 9, at lower Reynolds numbers, the RMS error between the model and Masters' experimental data grew to unsatisfactory levels.

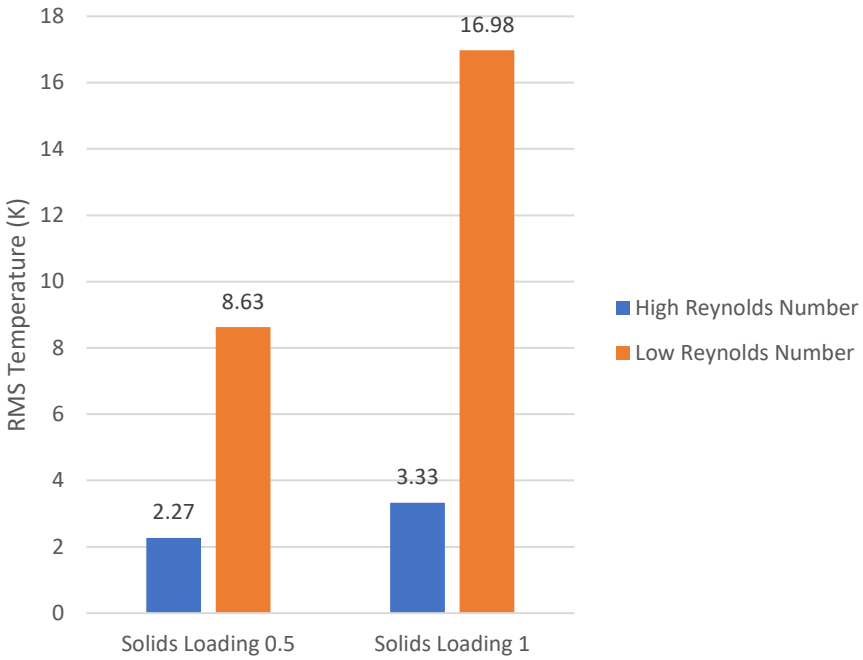


***Figure 9:*** *RMS temperature error between experimental results of Ref. [5] and the modeling effort of Ref. [4]*

The group tried to consider the reasons for the large RMS error at low Reynolds numbers and turned to the concentration profiles of solids that you can see below in figure 10. While Masters chose Reynolds numbers and solids loading ratio's to stay above the saltation velocity as defined by Rizk, the CFD model shows a tendency for particles to accumulate along the bottom of the test chamber. If particles truly are accumulating along the bottom of the test chamber than it would be incorrect to treat these particles the same as the dispersed particles. Attempting to account for these "settled" particles was the original motivation for this work.

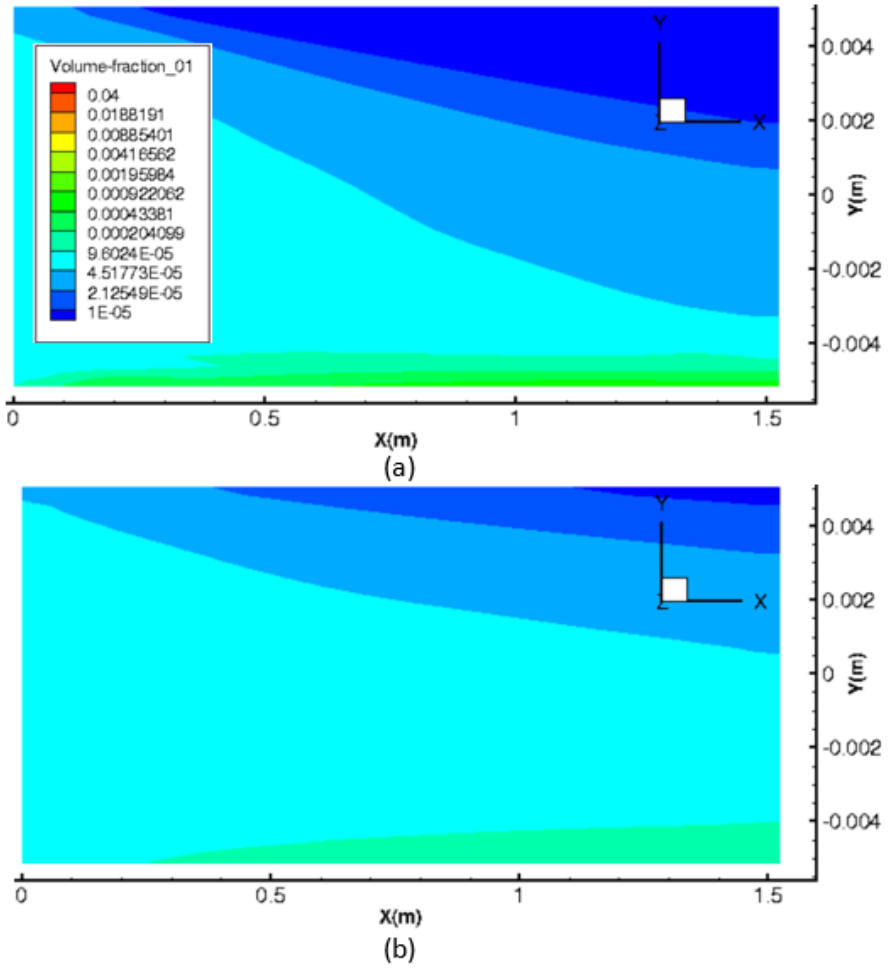


***Figure 10:*** *From Ref. [4] SL=1.0, 5 µm particle, volume fraction contour plots where:*
*(a) Reynolds number of* $3x10^4$
*(b) Reynolds number of* $6x10^4$

For the present work, this computational domain was further simplified in order to greatly reduce the computational burden while developing new models. This was done by converting the cylindrical domain into a flat channel flow between two wall boundaries with a pressure boundary on the end as can be seen in figure 11. The grid chosen was similarly simplified to be very coarse with 11 points in the x direction, 11 points in the y direction, and only 2 points in the z-direction. Ultimately it is the complicated physics that we are interested in for this Thesis, and simplifying the geometry promoted rapid fire

testing of developing models while maintaining the general characteristics of Masters' experiment. Future research will focus on mapping the new models to the original computational domain. This simple test domain can be seen below in figures 11-13.

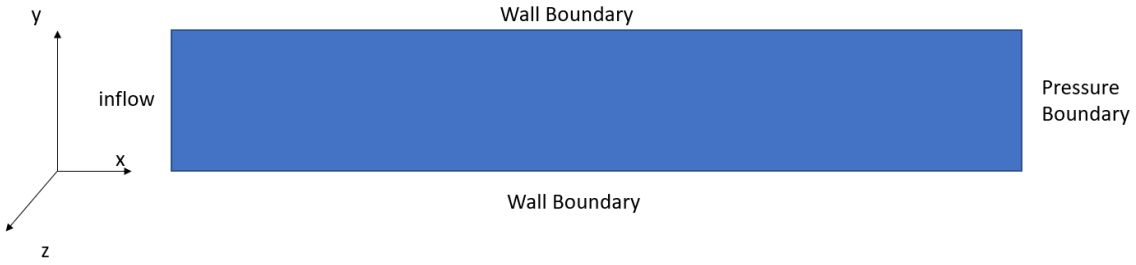


***Figure 11:*** *Simplified test domain.* $\frac{L}{H}$*=20 per Masters' experiment.*

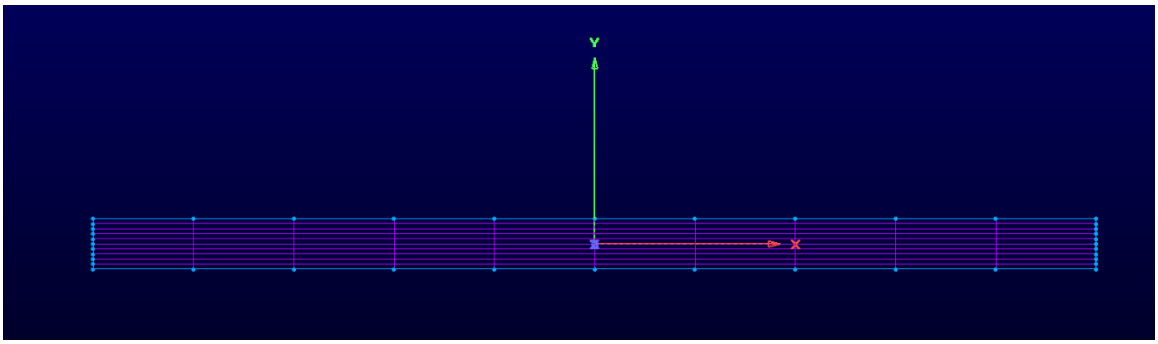


***Figure 12****: Axial grid distribution from simplified case. Ni=11 Nj=11*

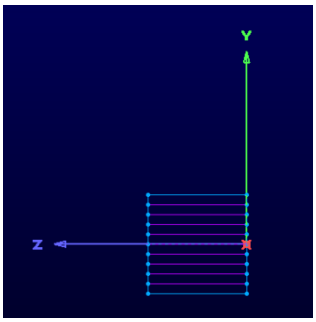


***Figure 13****: Cross section of computational domain. Nk=2*

## 3.2 Evolution of Baseline Model

Prior to developing new models utilizing the simplified test case described above, care was taken to recreate the work in Ref.[5]. Utilizing the computational domain shown above in figure's 6 and 7, the models in Ref.[5] were successively turned on for a 2 field (gas and particle phase) run. Each test run was post processed using ANSYS Ensight and plots were produced to ensure results were physical and matched expectations. The following pages will walk through the relevant plots and convergence histories for these incremental tests. The table below summarizes what models are enabled for the various test runs.

***Table 1**: Summary of parameters for test cases. α refers to volume fraction.*

| Computational Domain per Figures 6 and 7 | | | | | |
|---|---|---|---|---|---|
| Test A | | Test B | | Test C | |
| $\alpha_{inlet}$ Nitrogen | 0.999 | $\alpha_{inlet}$ Nitrogen | 0.999 | $\alpha_{inlet}$ Nitrogen | 0.999 |
| $\alpha_{inlet}$ Copper | 0.001 | $\alpha_{inlet}$ Copper | 0.001 | $\alpha_{inlet}$ Copper | 0.001 |
| Heat Flux | Off | Heat Flux | On | Heat Flux | On |
| Interfield Drag Model | On | Interfield Drag Model | On | Interfield Drag Model | On |
| Interfield Heat Transfer Model | Off | Interfield Heat Transfer Model | On | Interfield Heat Transfer Model | On |
| Dispersion Model | Off | Dispersion Model | Off | Dispersion Model | On |

Test A was an adiabatic run with only gravity and the inter-field drag model enabled. Results are shown below in figures 14-18. Figures 14 and 15 show that satisfactory convergence is achieved along with a reasonable velocity profile.

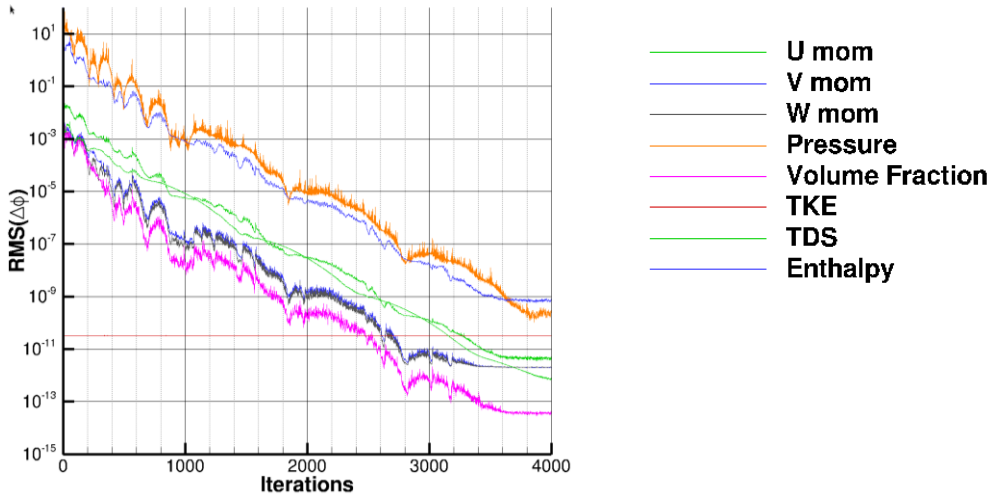


***Figure 14**: Convergence history for test A.*

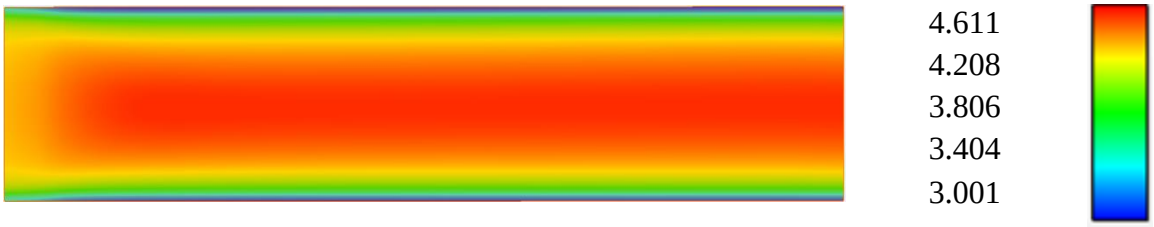


***Figure 15**: Nitrogen axial velocity for test A $\left[\frac{m}{s}\right]$.*


***Figure 16**: Nitrogen temperature for test A [°K].*


***Figure 17**: Dispersed copper temperature for test A [°K].*


***Figure 18**: Dispersed copper volume fraction.*

The next test run (Test B) included wall heat flux and modeled the inter-field heat transfer. Convergence as shown below in figure 19 was not as abrupt as for Test A but residuals decayed by several decades. For all future test runs, convergence was achieved similar to figures 14 or figure 19 and the histories are omitted. The Nitrogen axial velocity profile shown below matches expectations for a gas exposed to a wall heat flux. The temperature graphs shown below in figures 21 and 22 demonstrate that heat is being effectively transferred between the particles and the gas.

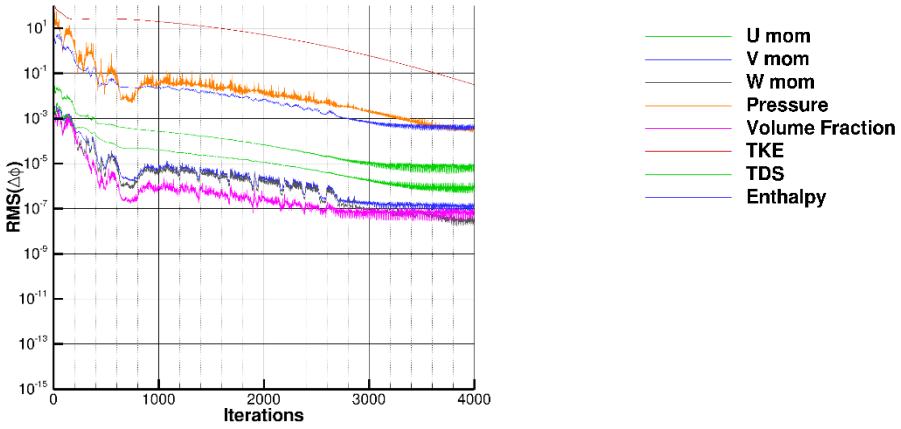


***Figure 19**: Convergence history for heated drag.*

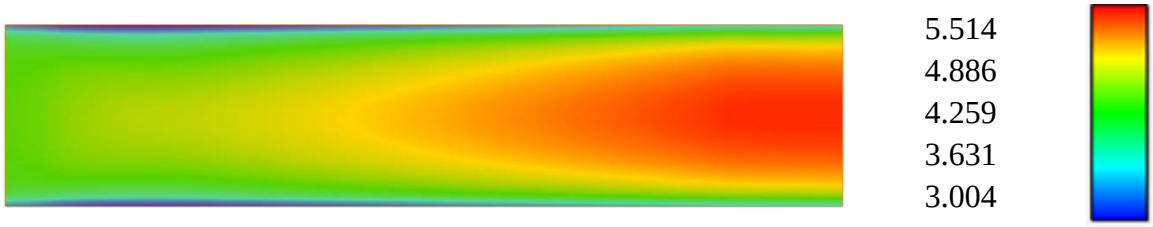


***Figure 20**: Nitrogen axial velocity for test B* $\left[\frac{m}{s}\right]$.

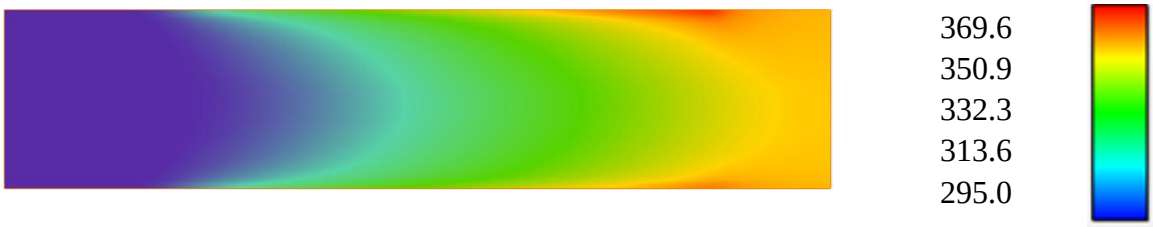


***Figure 21**: Nitrogen temperature for test B [°K]*

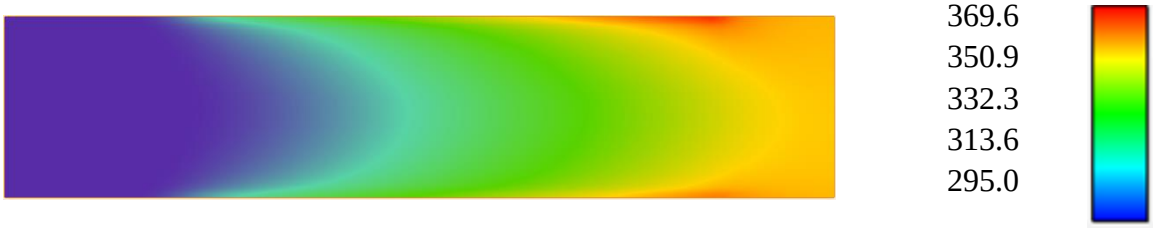


***Figure 22**: Dispersed copper temperature for test B [°K]*


***Figure 23**: Dispersed copper volume fraction for test B.*

Test C included heat transfer modeling as in Test B but added in turbulence dispersion modeling of the dispersed particle phase. Results are presented below.

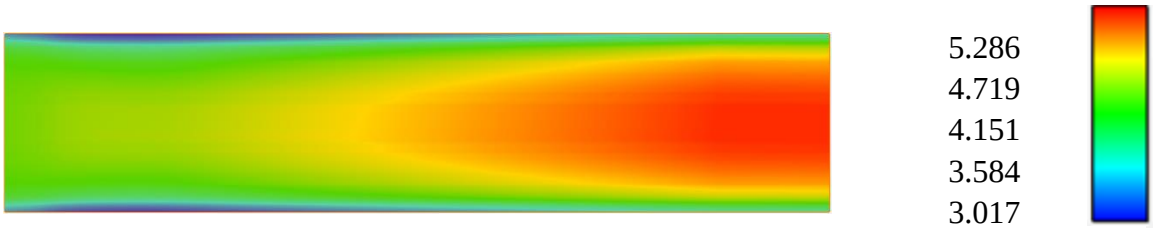


***Figure 24**: Nitrogen axial velocity for test C* $\left[\frac{m}{s}\right]$.

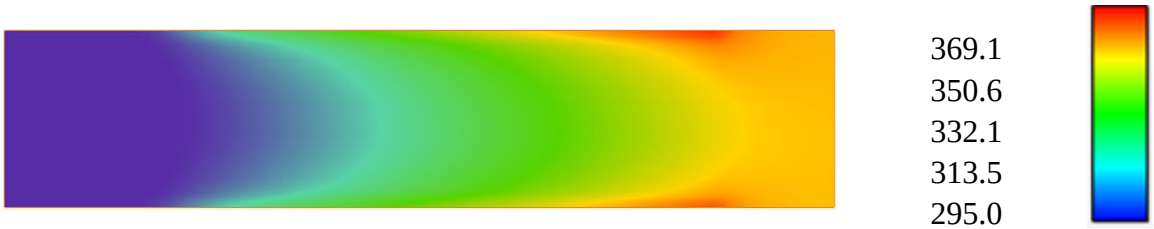


***Figure 25**: Nitrogen temperature for test C [°K].*

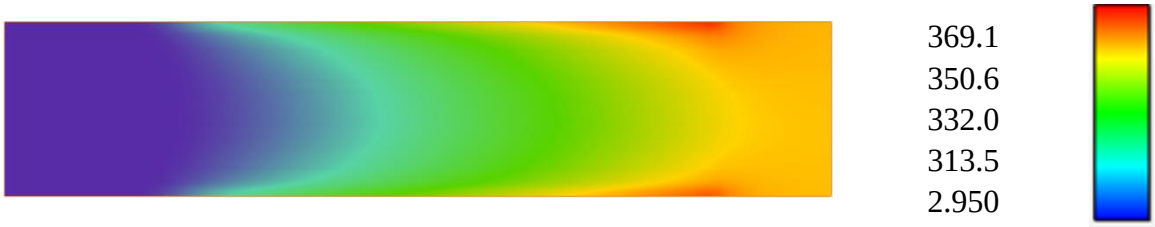


***Figure 26**: Dispersed copper temperature for Test C [°K].*

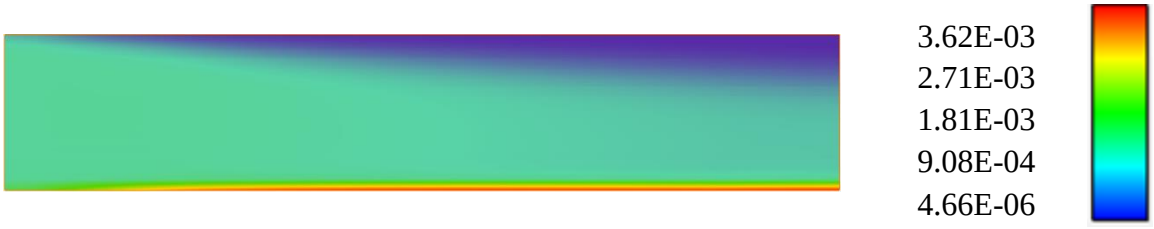


***Figure 27**: Dispersed particle volume fraction for test C.*

Referencing figures 24-27 above, there are only slight changes in the velocity and temperature profiles with the addition of turbulent dispersion, however there is a

noticeable change to the volume fraction profile as seen in figure 27. With dispersion modeled particle behavior due to turbulent oscillation within the flow channel is accounted for and the model predicts that particles will settled to the bottom of the flow channel. This behavior was modeled successfully in Ref.[5], but the settled particles were not treated any differently from the dispersed particles. As discussed in chapter 2, the drag and heat transfer treatment of particles settled on the bed of the channel and particles dispersed in the flow is very different. Developing and testing models for these settled particles was the motivation for this thesis.

### 3.3 Development of Models in Simplified Domain

There were too many variables at play in the computational domain described in figures 6 and 7 to properly develop and test new models. Additionally, the number of iterations required to reach convergence was growing to be a significant barrier as runs could take an hour or more. At this point the simplified domain described in figures 11-13 was introduced and a new baseline was established. The following pages will walk through the relevant plots highlighting the impact of each successive model in this simplified domain. The tables below lay out the difference between each test run.

***Table 2**: Summary of models in use for simplified test runs.*

| Computational Domain per Figures 11-13 | | | |
|---|---|---|---|
| Test D | | Test E | |
| $\alpha_{inlet}$ Nitrogen | 0.999 | $\alpha_{inlet}$ Nitrogen | 0.999 |
| $\alpha_{inlet}$ Copper | 0.001 | $\alpha_{inlet}$ Copper | 0.001 |
| $\alpha_{inlet}$ Copper Film | 0 | $\alpha_{inlet}$ Copper Film | 0 |
| Heat Flux | Off | Heat Flux | On |
| Interfield Drag Model | On | Interfield Drag Model | On |
| Interfield Heat Transfer Model | Off | Interfield Heat Transfer Model | Off |
| Dispersion Model | Off | Dispersion Model | Off |

***Table 3**: Summary of models in use for simplified test runs.*

| Computational Domain per Figures 11-13 | | | |
|---|---|---|---|
| Test F | | Test G | |
| $\alpha_{inlet}$ Nitrogen | 0.999 | $\alpha_{inlet}$ Nitrogen | 0.999 |
| $\alpha_{inlet}$ Copper | 0.001 | $\alpha_{inlet}$ Copper | 0.001 |
| $\alpha_{inlet}$ Copper Film | 0 | $\alpha_{inlet}$ Copper Film | 0 |
| Heat Flux | On | Heat Flux | On |
| Interfield Drag Model | On | Interfield Drag Model | On |
| Interfield Heat Transfer Model | On | Interfield Heat Transfer Model | On |
| Dispersion Model | Off | Dispersion Model | On |

Test D was an adiabatic test run with only the inter-field drag model enabled within the simplified domain. Results are presented below.

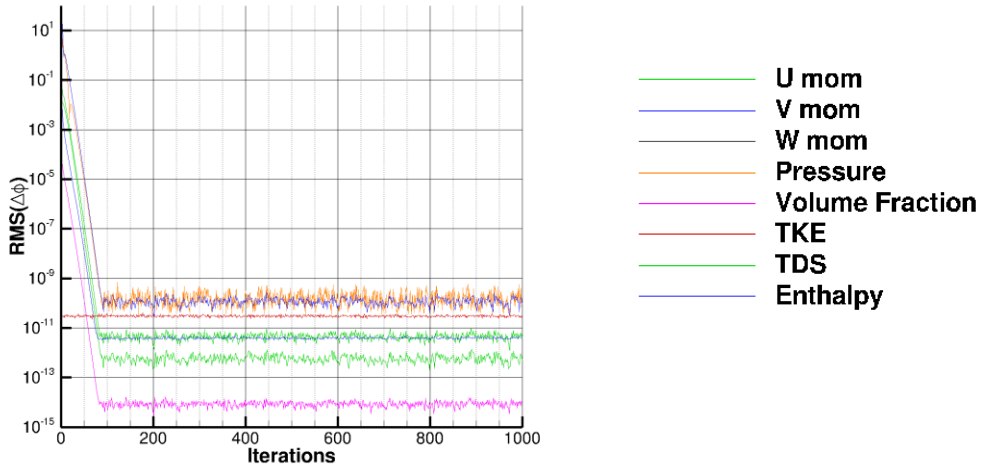


***Figure 28**: Convergence history for test D.*

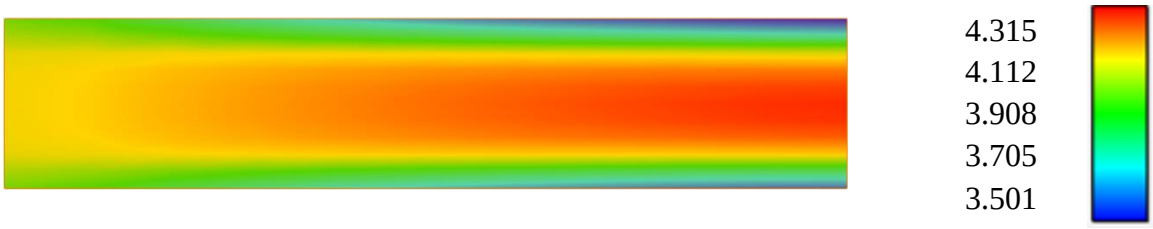


***Figure 29**: Nitrogen axial velocity for test D.* $\left[\frac{m}{s}\right]$

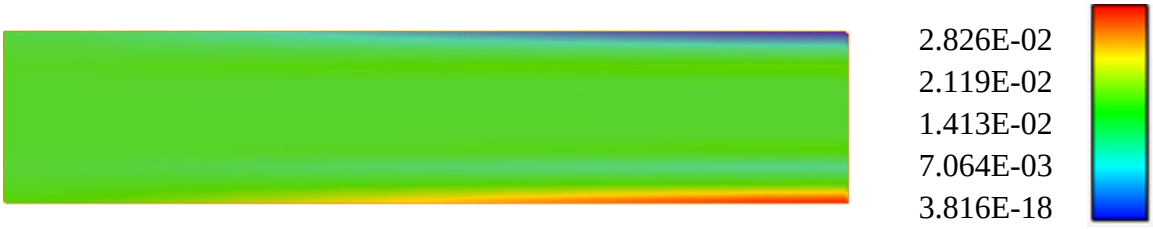


***Figure 30**: Dispersed particle volume fraction for test D.*

Referencing figures 28-30 above, the results match expectations for an adiabatic channel flow. Per figure 28, convergence was achieved in fewer than 400 iterations for the majority of the simplified tests. Convergence history plots are omitted from future tests unless there is a deviation from the behavior noted above in figure 28.

Test E enabled the wall heat flux but did not enable the inter-field heat transfer model. Results are presented below.

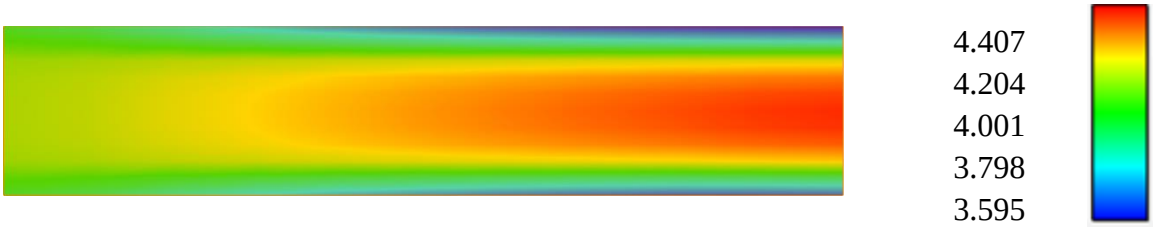


***Figure 31**: Nitrogen axial velocity for test E* $\left[\frac{m}{s}\right]$.

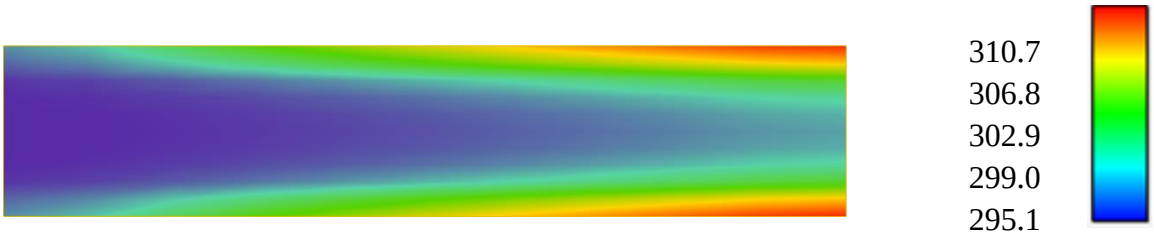


***Figure 32**: Nitrogen temperature for test E [°K].*


***Figure 33**: Dispersed copper temperature for test E [°K].*

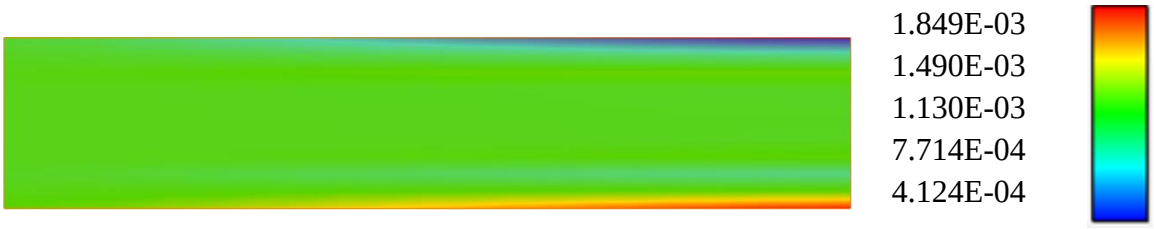


***Figure 34**: Dispersed copper volume fraction for test E.*

Figures 32 and 33 above show that dispersed particle phase temperature was constant as expected while the gas was heated by the wall heat flux.

In Test F, inter field heat transfer was enabled. The results can be seen below in figures 35-38. Figures 36 and 37 show that heat transfer from the gas to the dispersed solid phase is modeled effectively.

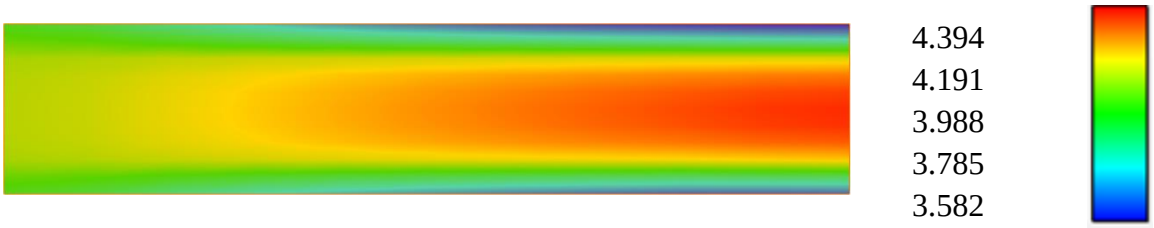


***Figure 35**: Nitrogen axial velocity for Test F $\left[\frac{m}{s}\right]$.*

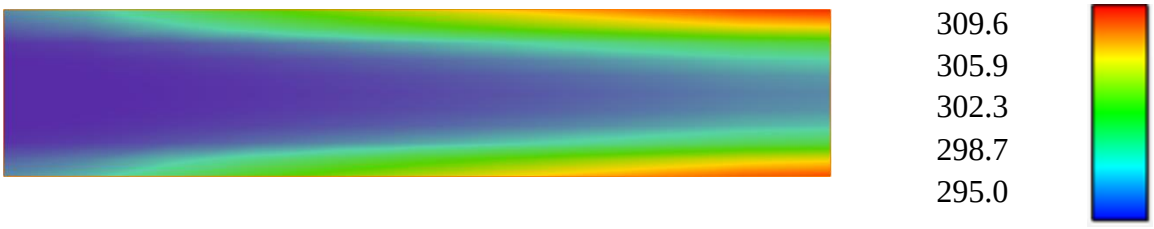


***Figure 36**: Nitrogen temperature for test F [°K].*

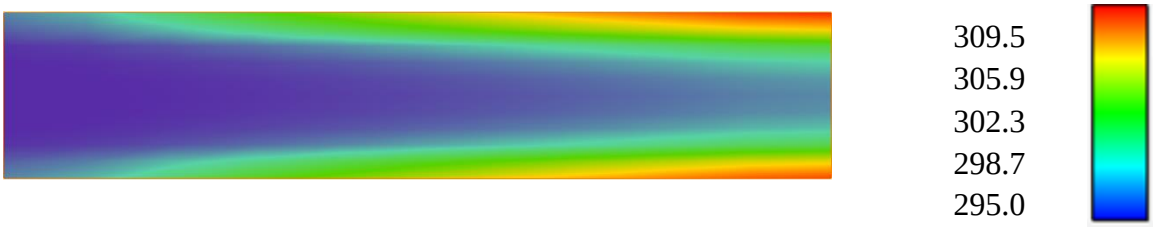


***Figure 37**: Dispersed copper temperature for test F [°K].*

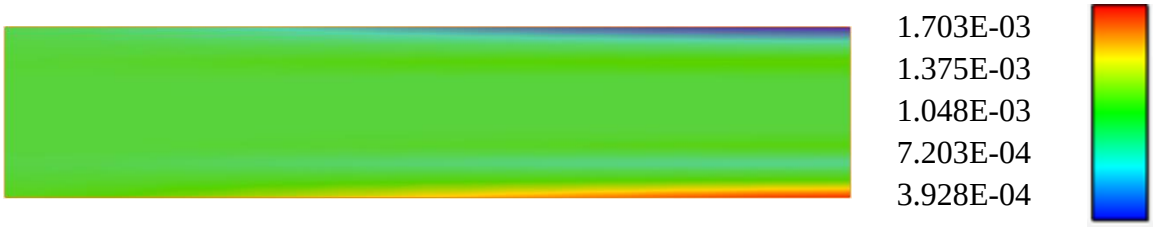


***Figure 38**: Dispersed particle volume fraction for test F.*

Test G added the turbulence dispersion model to the simplified domain. Results are presented below.

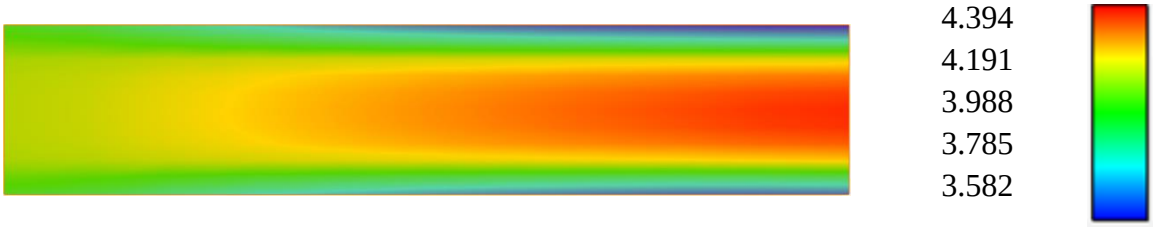


***Figure 39**: Nitrogen axial velocity for test G $\left[\frac{m}{s}\right]$.*

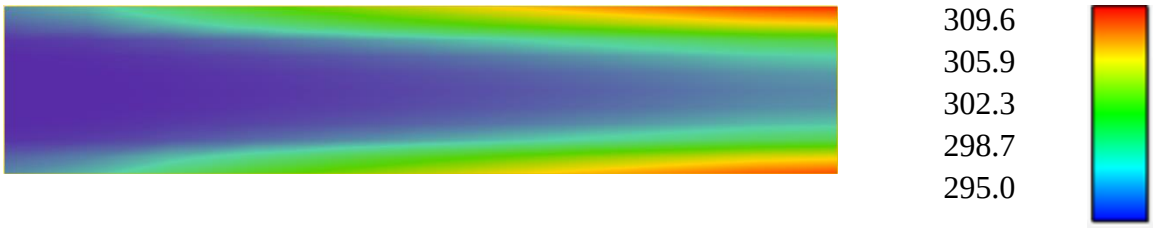


***Figure 40**: Nitrogen temperature for test G [°K].*

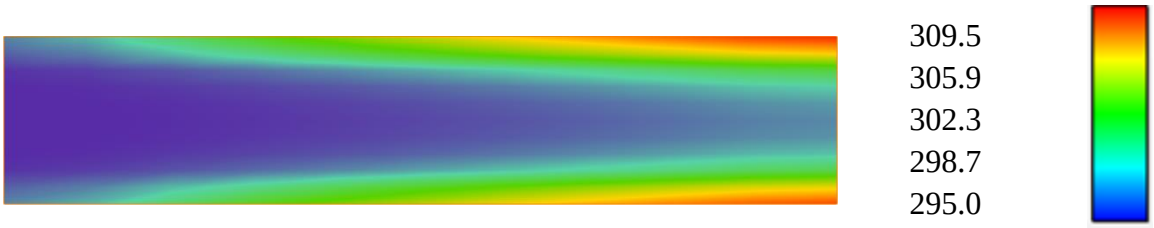


***Figure 41**: Dispersed Copper temperature for test G [°K].*

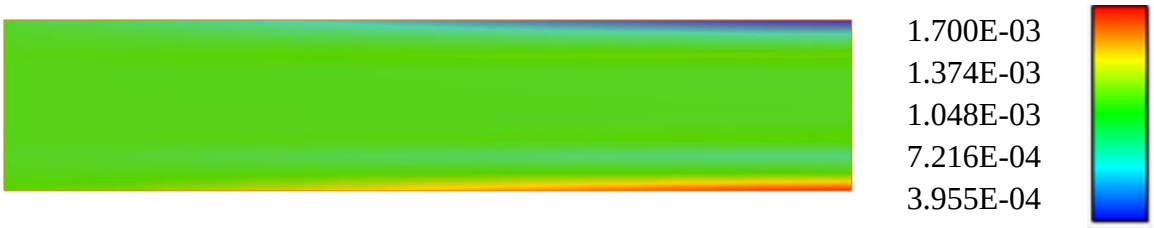


***Figure 42**: Dispersed particle volume fraction for test G.*

The addition of the turbulence dispersion model had a slight impact of the volume fraction of the dispersed particles but the other profiles were mostly unaffected. Figure 42 shows that the behavior observed previously in figure 27 of particles collecting on the bottom of the flow channel is still present. This behavior means that the simplified domain still exhibits the same behavior witnessed in Test C that justifies the need for model improvements to account for particle settling.

With the drag, heat transfer and turbulence dispersion models functioning as expected in the simplified computation domain, it was time to add in the particle film layer. In order to isolate the impact of the new models, a new three field baseline was established by conducting the initial three field test runs adiabatically with inter-field heat transfer and turbulence dispersion models turned off. The initial volume fraction for the film was chosen to be very small such that we expected no discernible change between the 2 phase run (Test D per table 2 and figures 28-30) and the three phase run (test H).

The parameters chosen for baseline test H are summarized below in table 4. Two numbers are presented for inter-field drag where the first number refers to the model used for the dispersed particle phase, and the second number refers to the model used for the film phase. In Test H, both the dispersed and film fields utilized the same smooth spherical particle model [20] (denoted as model 3 in the table). Results are presented below.

***Table 4:*** *Summary of models used for baseline three field test run*

| Computational Domain per figure 11-13 | |
|---|---|
| Test H | |
| $\alpha_{inlet}$ Nitrogen | 0.99899999999 |
| $\alpha_{inlet}$ Copper | 0.001 |
| $\alpha_{inlet}$ Copper Film | 0.00000000001 |
| Heat Flux | Off |
| Inter-field Drag Model (Dispersed phase, Film phase) | 3, 3 |
| Interfield Heat Transfer Model | Off |
| Dispersion Model | Off |

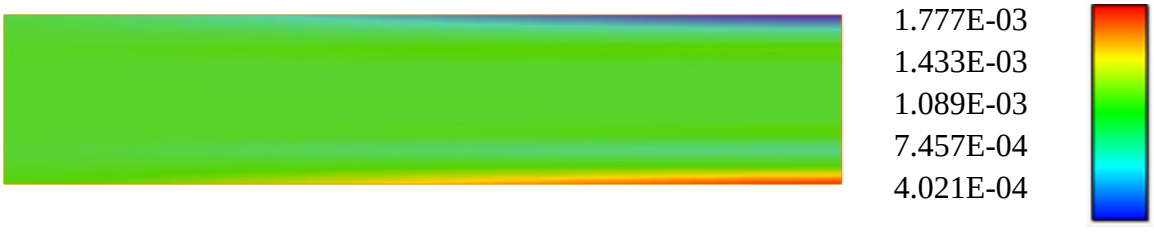


***Figure 43****: Dispersed particle volume fraction for test H.*

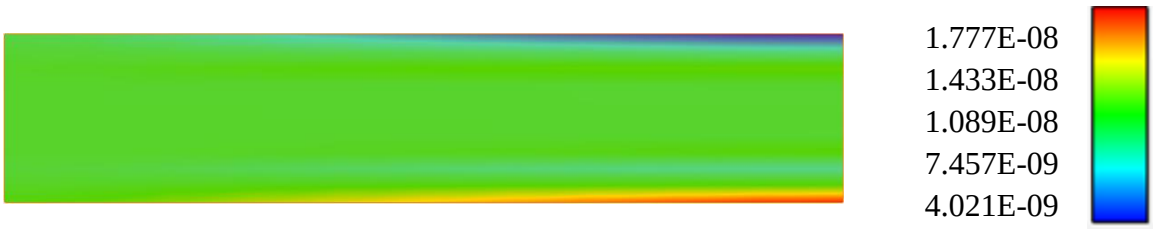


***Figure 44**: Particle film volume fraction for test H.*

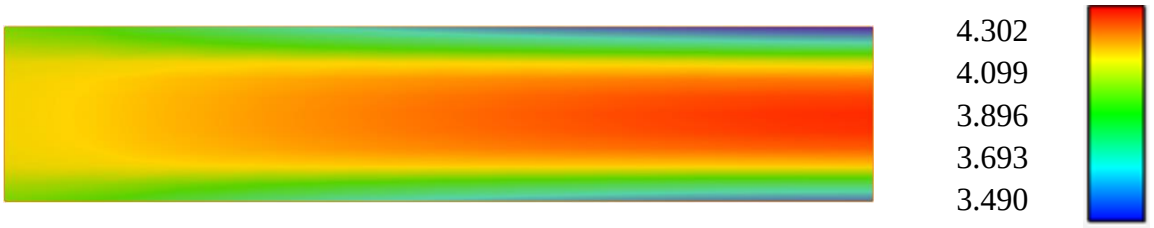


***Figure 45:** Nitrogen axial velocity for test H* $\left[\frac{m}{s}\right]$.

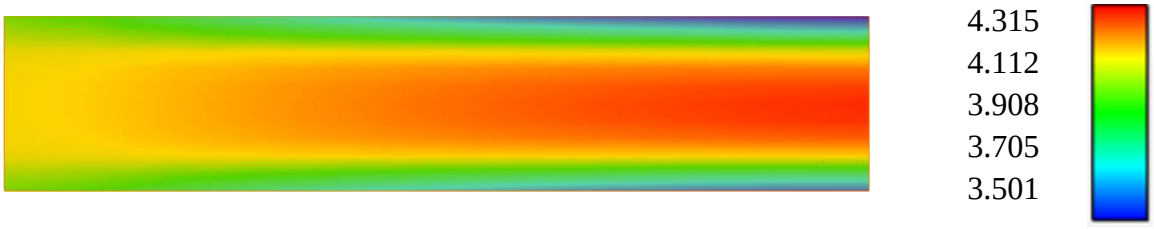


***Figure 46**: Nitrogen axial velocity for test D.* $\left[\frac{m}{s}\right]$ *Presented again for convenience.*

The results matched expectations as can be seen above by comparing figures 45 and 46. The slight difference in velocities is likely a result of the small change in volume fraction due to the addition of the third field.

At this point the new drag model (denoted drag model 15) was introduced. This model properly accounts for the shear force that the particle film layer exerts on the gas phase in order to predict a more accurate velocity field. For a more detailed breakdown of

this drag model refer back to chapter 2. This new model was tested using the same adiabatic conditions as Test H. Refer to Table 5 for a reference of the models used. The results are presented below.

***Table 5:*** *Summary of models used for test I.*

| Computational Domain per figure 11-13 | |
|---|---|
| Test I | |
| $\alpha_{inlet}$ Nitrogen | 0.99899999999 |
| $\alpha_{inlet}$ Copper | 0.001 |
| $\alpha_{inlet}$ Copper Film | 0.00000000001 |
| Heat Flux | Off |
| Inter-field Drag Model (Dispersed phase, Film phase) | 3,15 |
| Interfield Heat Transfer Model | Off |
| Dispersion Model | Off |

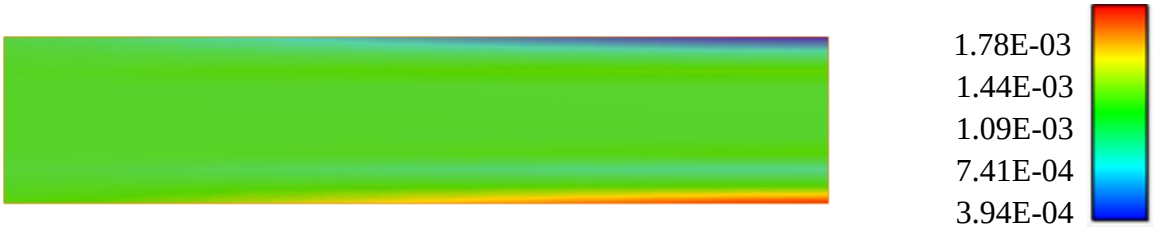


***Figure 47****: Dispersed copper volume fraction for test I.*

Referencing figure 47 above, notice that even with the new drag model for the film, the dispersed particles still tend to settle. This means that as in Test C, the new drag model is capturing the behavior of particle settling that helped motivate this thesis.


***Figure 48**: Copper film volume fraction for test I.*

Figure 48 above seems to present a strange result. We would expect the copper film particles to flow along the bottom of the channel and concentrate at the bottom right of the figure above. This non-physical result is likely explained by the very small volume fraction assigned for the copper film. As there is effectively zero film, volume fraction plot can be considered anomalous.

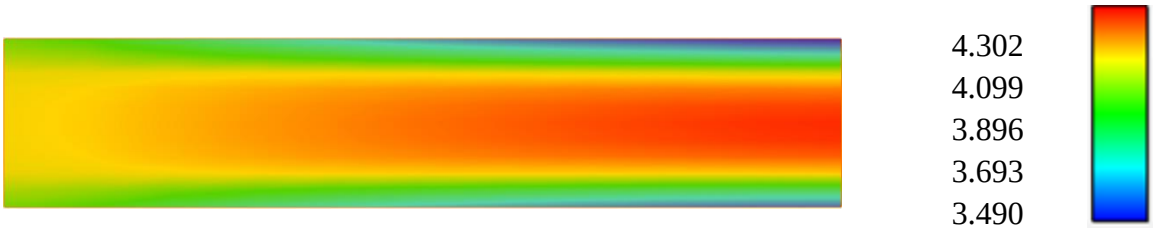


***Figure 49**: Nitrogen axial velocity for test I $\left[\frac{m}{s}\right]$. Notice the similarity to Test H presented below for convenience.*

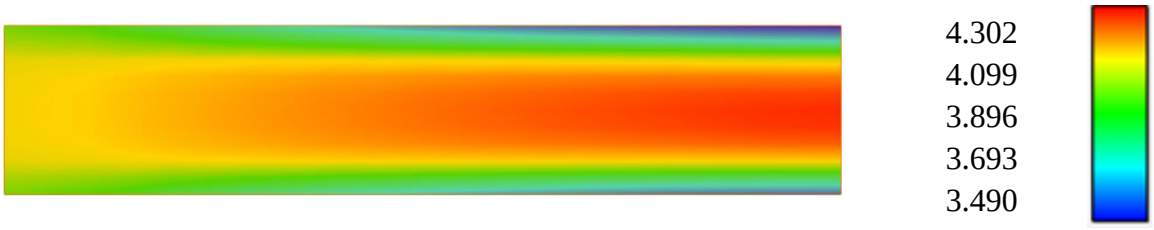


***Figure 50**: Nitrogen axial velocity for Test H $\left[\frac{m}{s}\right]$. Presented again for convenience*

Figures 49 and 50 show nearly identical results for Nitrogen axial velocity when compared to the two field case (Test D). In fact, the Nitrogen axial velocity computed in Test I with the new drag model (model 15) is identical to the velocities computed in test

H with the old drag model. As previously mentioned, this was the expected outcome given that there was a particle film layer volume fraction of $1x10^{-11}$ which means there is effectively no film present.

The plots above provide confidence that the new drag model is functioning as expected however in order to further validate the new drag model, we ran additional tests with increased film volume fractions. The table below summarized the parameters of these additional tests.

***Table 6:*** *Summary of models used to validate new drag model (model 15).*

| Computational Domain per Figures 11-13 | | | |
|---|---|---|---|
| Test J | | Test K | |
| $\alpha_{inlet}$ Nitrogen | 0.99899 | $\alpha_{inlet}$ Nitrogen | 0.998 |
| $\alpha_{inlet}$ Copper | 0.001 | $\alpha_{inlet}$ Copper | 0.001 |
| $\alpha_{inlet}$ Copper Film | 0.00001 | $\alpha_{inlet}$ Copper Film | 0.001 |
| Heat Flux | Off | Heat Flux | Off |
| Inter-field Drag Model (Dispersed phase, Film phase) | 3, 15 | Inter-field Drag Model (Dispersed phase, Film phase) | 3, 15 |
| Inter-field Heat Transfer Model | Off | Inter-field Heat Transfer Model | Off |
| Dispersion Model | Off | Dispersion Model | Off |

Test J raised the film volume fraction from $10^{-11}$ to $10^{-5}$. Results for Test J are presented below.

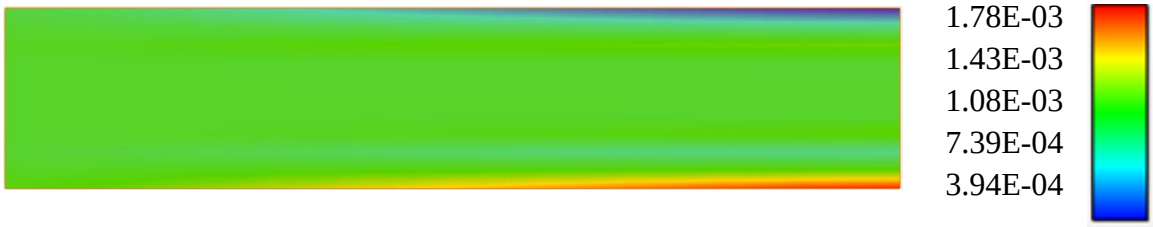


***Figure 51**: Dispersed particle volume fraction for test J.*


***Figure 52**: Copper film volume fraction for test J.*

Figures 51 and 52 above show the volume fractions for dispersed particle phase and particle film phase respectively. The dispersed particle phase reflects the same trend pointed out for previous tests where particles tend to concentrate on the bottom of the flow channel. Unlike test I, the copper film volume fraction from Test J does match expectations in that particles accumulate at the end of the flow channel. Whereas Test I had effectively zero film, Test J has an appreciable amount of film giving the models something to work with. This model behavior will be worth keeping in mind if the models are ever extended for additional use cases.

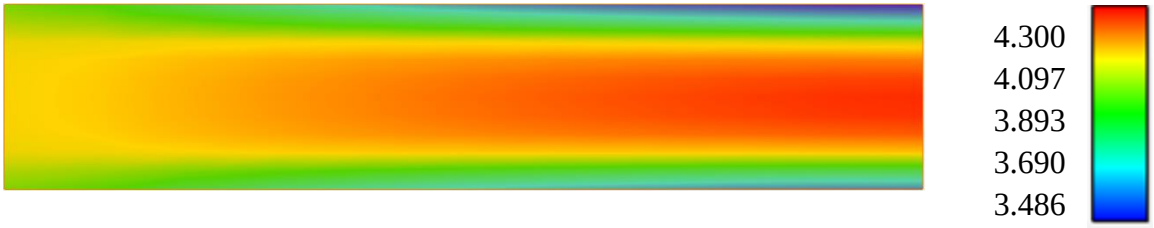


**Figure 53**: Nitrogen axial velocity for test J $\left[\frac{m}{s}\right]$.

Figure 53 above shows results that appear similar to Test I at first glance, but notice that the Nitrogen axial velocities are slightly lower than those presented for Test I in figure 49. This matches expectations as more film implies more film drag which would lower the flow velocity.

Test K matches the dispersed particle and particle film volume fractions. We would expect a more noticeable film drag effect in this test. Results are presented below.

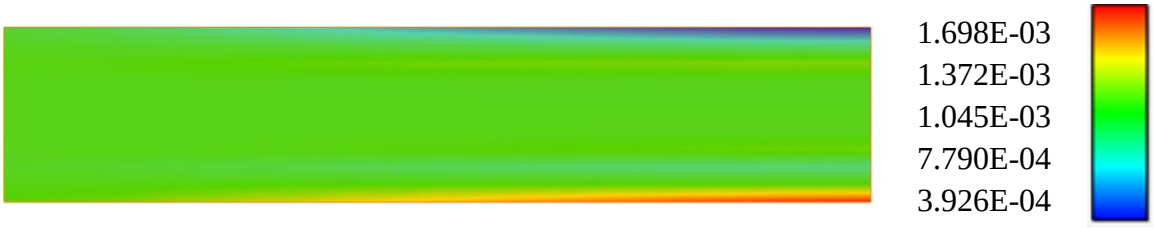


***Figure 54**: Dispersed particle volume fraction for test K.*


***Figure 55**: Copper film volume fraction for test K.*

As in Test J, figures 54 and 55 show the same trend observed previously with the buildup of particles along the bottom of the flow channel. If accurate, this buildup continues to provide justification for the present work.

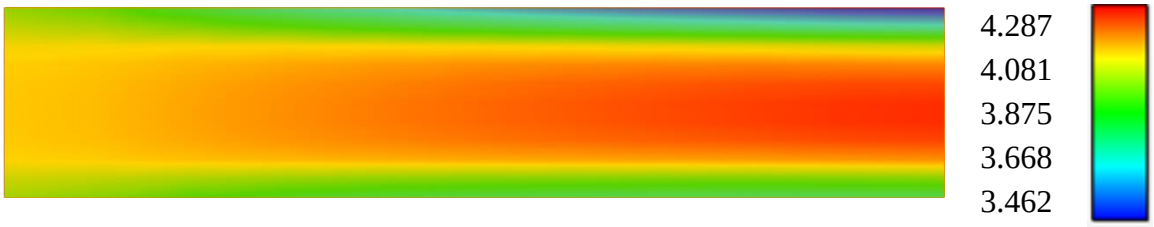


***Figure 56**: Nitrogen axial velocity for test K* $\left[\frac{m}{s}\right]$.

Figure 56 above continues the trend observed in Test J. Nitrogen axial velocity has fallen further when compared to tests I or J indicating that the additional film is producing more drag on the flow. There is also a significant drop in the Nitrogen axial velocity at the top of the top right of figure 56. This is best explained by considering that it is $\alpha u$ that is conserved (where $\alpha$ is volume fraction and $u$ is velocity). Figure 54 above shows that the volume fraction of dispersed particles is falling in the top region which means that the volume fraction of the Nitrogen in this region must be going up. If the volume fraction of Nitrogen increases, then the velocity must decrease when conserving $\alpha u$.

## 3.4 Mass Transfer in the Simplified Domain

The final model implemented and tested was the mass transfer model. The mass transfer model presented and evaluated below accounts for the sedimentation/impaction and the diffusion which causes mass transfer from the dispersed particle phase to the continuous particle film phase. The physics of this model is discussed in detail in chapter 2. Future researchers will need to implement the mass transfer model accounting for the

re-entrainment of particles from the continuous particle film to the dispersed particle phase. The table below presents the parameters used for the test.

***Table 7:*** *Parameters used for mass transfer test.*

| Computational Domain per Figures 11-13 | |
|---|---|
| Test L | |
| $\alpha_{inlet}$ Nitrogen | 0.99899999999 |
| $\alpha_{inlet}$ Copper | 0.001 |
| $\alpha_{inlet}$ Copper Film | 0.00000000001 |
| Heat Flux | Off |
| Inter-field Drag Model (Dispersed phase, Film phase) | 3, 15 |
| Inter-field Heat Transfer Model | Off |
| Dispersion Model | Off |
| Mass Transfer | On |

The initial copper film volume fraction was set to $1x10^{-11}$ which is effectively zero. This exactly matches the parameters used above in Test I with the exception of the mass transfer model. If the mass transfer model behaves as expected, there should be a noticeable difference in the volume fraction of the dispersed particles and the copper film as you move through the flow channel. The results of Test L are presented below.

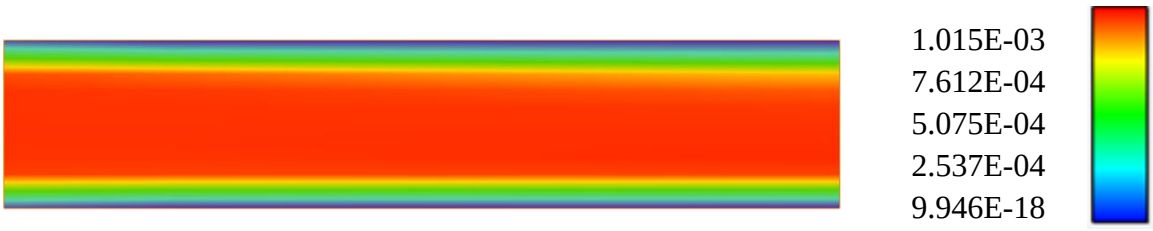


***Figure 57****: Dispersed particle volume fraction for test L.*


***Figure 58**: Copper film volume fraction for test L.*

When referencing figures 57 and 58 above, the first thing to note is the mass transfer between the two fields. The volume fraction profile for the copper film presented in figure 58 shows a clear accumulation of particles along the flow channel matching expectations. Furthermore, the order of magnitude of the volume fraction shows a noticeable increase in volume fraction from the seeded $1x10^{-11}$ for the test. Figure 57 showing the dispersed particle phase volume fraction shows a reduction in concentration along the bottom of the flow channel which matches expectations. Physically this represents the sedimentation/impaction along with diffusion discussed in chapter 2. The reduction in volume fraction along the top of the flow channel is likely non-physical and will require further debugging. As the model stands right now, it seems to not be differentiating between the top and the bottom of the flow channel.

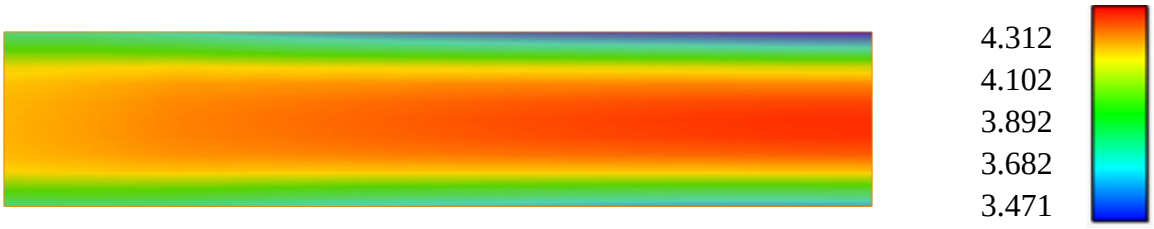


***Figure 59:*** *Nitrogen axial velocity for test L* $\left[\frac{m}{s}\right]$.

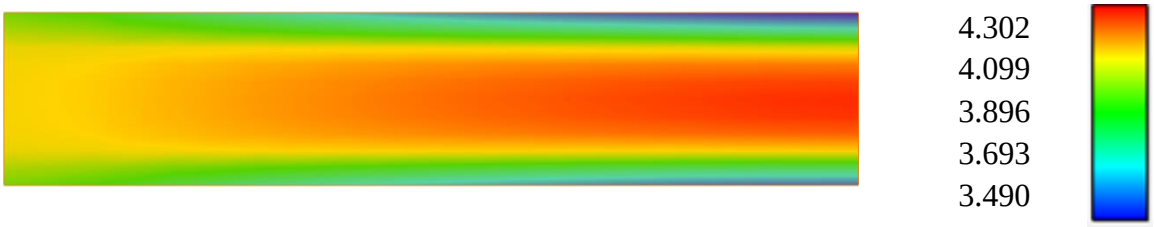


***Figure 60:*** *Nitrogen axial velocity for Test I* $\left[\frac{m}{s}\right]$. *Presented again for convenience.*

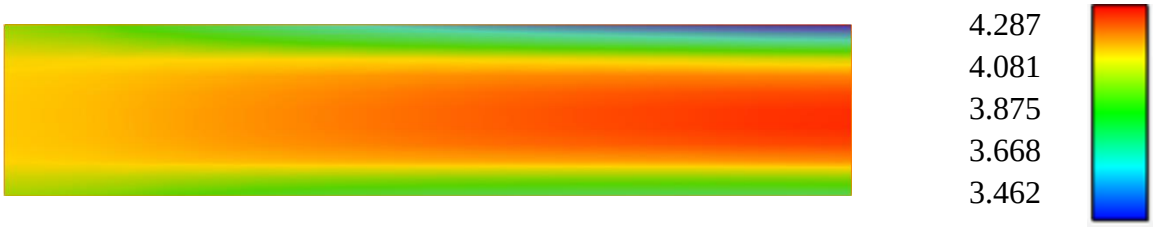


***Figure 61****: Nitrogen axial velocity for Test K* $\left[\frac{m}{s}\right]$. *Presented again for convenience.*

From figure 59 above, notice that the velocity profile appears to be a mixture of the profile presented in Test I (figure 60) which had very little film and the profile presented in Test K (figure 61) which had significant film. More specifically, the low-end velocity for Test L of 3.471 $\left[\frac{m}{s}\right]$ is between the low-end velocity for Test I (3.490 $\left[\frac{m}{s}\right]$ )

and the low-end velocity for test K (3.462 $\left[\frac{m}{s}\right]$ ). This result matches expectations given that there should be significantly more film present in Test L than there was in Test I, but on average there would be less film present than there was in Test K. One strange behavior is that the high-end velocity for Test L (4.312 $\left[\frac{m}{s}\right]$) is higher than for both Test I (4.302 $\left[\frac{m}{s}\right]$) and Test K (4.287 $\left[\frac{m}{s}\right]$). This could be an artifact of how $\alpha u$ is conserved as previously mentioned but will need to be explored further and validated against experimental data.

## 3.4 Implementation of New Models

After validating the models in isolation, all previously mentioned models were re enabled to see if the results held up. Table 8 below summarizes the parameters used for this test and the results are found below in figures 66-70.

***Table 8:*** *Summary of models used for final validation.*

| Computational Domain per figure 11-13 | |
|---|---|
| Test M | |
| $\alpha_{inlet}$ Nitrogen | 0.99899999999 |
| $\alpha_{inlet}$ Copper | 0.001 |
| $\alpha_{inlet}$ Copper Film | 0.00000000001 |
| Heat Flux | On |
| Inter-field Drag Model (Dispersed phase, Film phase) | 3, 15 |
| Inter-field Heat Transfer Model (dispersed phase only) | On |
| Dispersion Model | On |
| Mass Transfer | On |

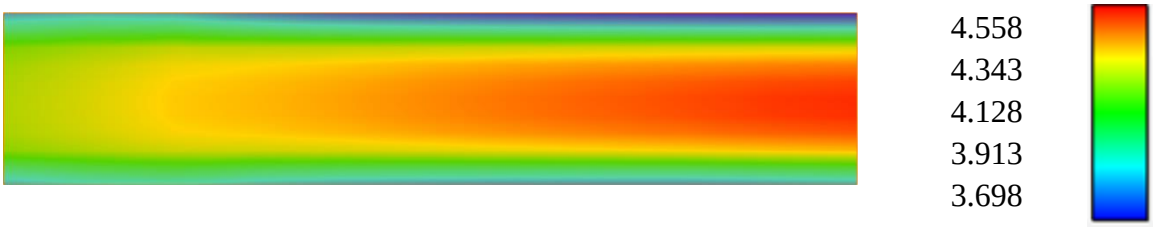


***Figure 62**: Nitrogen axial velocity for test M.* $\left[\frac{m}{s}\right]$

Figure 62 above shows similar behavior observed in test L (figure 59). The asymmetry of the Nitrogen axial velocity showing the slowing down along the top of the flown channel seems to be characteristic of the new drag model. The flow is sped up compared to test L which matches expectations given that flow is now exposed to heating.

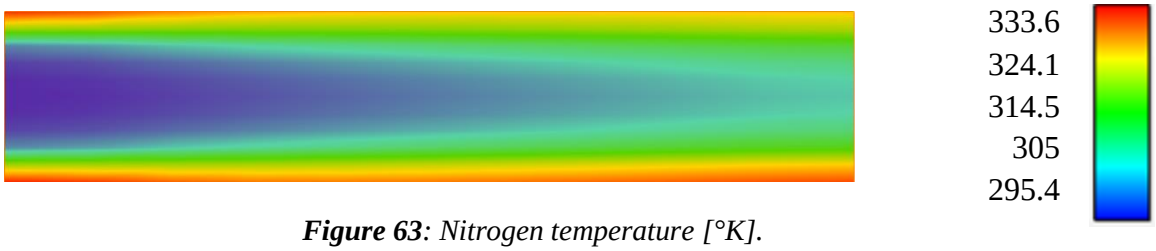


***Figure 63**: Nitrogen temperature [°K].*

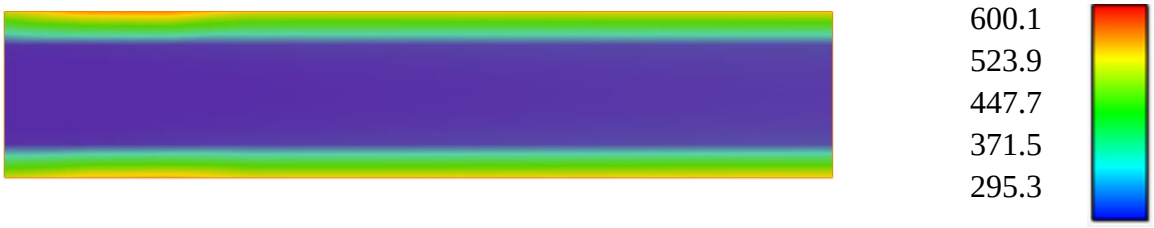


***Figure 64**: Dispersed copper temperature [°K].*

Figures 63 and 64 above show the temperature profiles for the Nitrogen gas phase and the dispersed copper phase respectively. The profile presented in figure 63 matches expectations for a developed flow exposed to wall heating, however the dispersed copper temperature profile in figure 64 is not physical. This non-physicality could be a result of accounting for the mass transfer from the dispersed phase to the film phase without accounting for the heating impact of the additional film phase. The implementation and testing of the heat transfer model for the film phase as discussed in chapter 2 will be a priority for future work. Additional debugging may be required if the profile presented in figure 68 remains after accounting for the film heating.

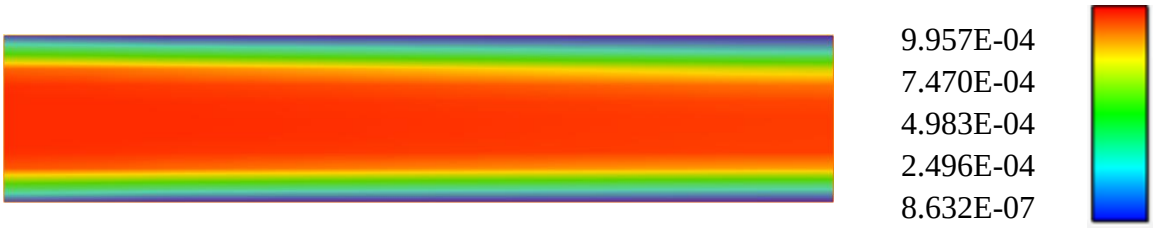


***Figure 65**: Dispersed copper volume fraction.*


***Figure 66:** Copper film volume fraction.*

Figures 65 and 66 above closely match figures 57 and 58 from test L. Mass transfer from the dispersed phase to the film phase is clearly visible when referencing figures 65 and 66. Like in test L, there seems to be a nonphysical loss of particulate along the top of the flow channel for the dispersed particle phase (figure 65).

# Chapter 4 Conclusions and Future Work

This thesis extended the work of Ref. [5] by adding a third field which represented the settled bed of particles that was observed in Ref. [6]. A simplified computational domain was proposed to aide in the development and testing of the new models required for this additional particle film field. A new model for the drag between the particle film and the carrier gas field was developed and tested and showed physically correct results when tested in the simplified domain. A mass transfer model which accounted for the sedimentation/impaction and the diffusion of the dispersed particle phase into the particle film phase was developed and tested and the expected buildup of particles into the film phase was observed in the simplified model.

When models were tested alongside the models of Ref. [4], results matched expectations with a key exception being the temperature profile of the dispersed particle phase. The non-physical profile presented above in figure 68 was hypothesized to be a result of failing to model the heating of the film phase. The implementation and testing of the proposed model from chapter 2 will be a priority for future work.

The literature surveyed for this thesis suggested that there should be additional mass transfer from the particle film field to the dispersed particle phase as a result of the saltating motion of the particles exposed to a shearing force. This behavior was not modeled in the present work, but a potential model was presented in chapter 2. Alongside accounting for the heating of the film, the implementation and testing of this model is the next logical step to fully capture the behavior in the experiments from Ref. [6].

Once the models presented in this work are debugged, and the proposed models are implemented, significant work remains in testing the models. The Nusselt number predicted by the code must be analyzed and compared to the Nusselt numbers predicted in Ref. [4]. This analysis will ultimately determine whether or not the improved models are effective at predicting heat transfer performance of particle laden flows. For the time being, Masters' experiment of Ref. [6] is the primary dataset for comparison In the event that the predictive capability of this code is an improvement over the work in Ref. [4], future work could involve developing new experiments with different parameters. The models presented in this Thesis could then be validated against additional data sets, providing further confidence in their accuracy. Once the models prove robust enough, they could be deployed in place of experiments to provide engineers and researchers a low-cost approximation of the heat transfer performance of a particle-laden flow.

# References

[1] Yannopoulos, J. C., Themelis, N. J., and Gavvin, W. H., 1966, "An Evaluation of the Pneumatic Transport Reactor," Can. J. Chem. Eng., **44**(4), pp. 231–235.

[2] Boothroyd, R. G., 1969, "Heat Transfer in a Gas Borne Suspension of Fine Particles in Turbulent Duct Flow," Appl. Sci. Resour., **21**(1), pp. 98–112.

[3] Buongiorno, J., and Hu, L. W., 2009, "Nanofluid Heat Transfer Enhancement for Nuclear Reactor Applications," *Proceedings of the ASME Micro/Nanoscale Heat and Mass Transfer International Conference 2009, MNHMT2009*, Shanghai, pp. 517–522.

[4] Farbar, L., and Morley, M., 1957, "Heat Transfer to Flowing Gas-Solids Mixtures in a Circular Tube," Ind. Eng. Chem., **49**(7), pp. 1143–1150.

[5] Hassan, K., Kunz, R., Hanson, D., and Manahan, M., 2020, "A Numerical Investigation into the Heat Transfer Performance and Particle Dynamics of a Compressible, Highly Mass Loaded, High Reynolds Number, Particle Laden Flow," *ASME 2020 Heat Transfer Summer Conference*, p. in print.

[6] Masters, S. R., 2018, "Effect of Particle Concentration and Reynolds Number on Heat Transfer in Particle-Laden Flows," The Pennsylvania State University.

[7] Whitaker, S., 1972, "Forced Convection Heat Transfer Correlations for Flow in Pipes, Past Flat Plates, Single Cylinders, Single Spheres, and for Flow in Packed Beds and Tube Bundles," AIChE J., **18**(2), pp. 361–371.

[8] Muley, A., and Manglik, R. M., 1999, “Experimental Study of Turbulent Flow Heat Transfer and Pressure Drop in a Plate Heat Exchanger with Chevron Plates,” Trans. ASME, **121**, pp. 69–76.

[9] Vicente, P. G., García, A., and Viedma, A., 2002, “Heat Transfer and Pressure Drop for Low Reynolds Turbulent Flow in Helically Dimpled Tubes,” Int. J. Heat Mass Transf., **45**(3), pp. 543–553.

[10] Farbar, L., and Depew, C. A., 1963, “Heat Transfer Effects to Gas-Solids Mixtures Using Solid Spherical Particles of Uniform Size,” Ind. Eng. Chem. Fundam., **2**(2), pp. 130–135.

[11] Depew, C. A., and Farbar, L., 1963, “Heat Transfer to Pneumatically Conveyed Glass Particles of Fixed Size,” J. Heat Transfer, **85**(2), pp. 164–171.

[12] Depew, C. A., 1960, “Heat Transfer to Flowing Gas- Solids Mixtures in a Vertical Circular Duct,” University of California, Berkeley.

[13] Kane, R. S., and Pfeffer, R., 1985, “Heat Transfer in Gas-Solids Drag- Reducing Flow,” Trans. ASME, **107**, pp. 570–574.

[14] Kim, J. M., and Seader, J. D., 1983, “Heat Transfer to Gas-Solids Suspensions Flowing Concurrently Downward in a Circular Tube,” AIChE J., **29**(2), pp. 306–312.

[15] Tien, C. L., 1961, “Heat Transfer by a Turbulently Flowing Fluid-Solids Mixture in a Pipe,” J. Heat Transfer, **83**(2), pp. 183–188.

[16] Boothroyd, R. G., and Hague, H., 1970, “Fully Developed Heat Transfer to a Gaseous Suspension of Particles Flowing Turbulently in Ducts of Different Size,” J. Mech. Eng. Sci., **12**(3), pp. 191–200.

[17] Han, K. S., Sung, H. J., and Chung, M. K., 1991, “Analysis of Heat Transfer in a Pipe Carrying Two-Phase Gas-Particle Suspension,” Int. J. Heat Mass Transf., **34**(1), pp. 69–78.

[18] Liu, C., Tang, S., Shen, L., and Dong, Y., 2017, “Characteristics of Turbulence Transport for Momentum and Heat in Particle-Laden Turbulent Vertical Channel Flows,” Acta Mech. Sin. Xuebao, **33**(5), pp. 833–845.

[19] Kuerten, J. G. M., van der Geld, C. W. M., and Geurts, B. J., 2011, “Turbulence Modification and Heat Transfer Enhancement by Inertial Particles in Turbulent Channel Flow,” Phys. Fluids, **23**(12), p. 123301.

[20] Schiller, L., and Naumann, A., 1935, “A Drag Coefficient Correlation,” Z. Ver. Deutch. Ing., **77**, pp. 318–320.

[21] Lopez De Bertodano, M. A., 1998, “Two Fluid Model for Two-Phase Turbulent Jets,” Nucl. Eng. Des., **179**(1), pp. 65–74.

[22] Gilbert, G. K., 1914, *The Transportation of Debris by Running Water*, 86, Washington, D. C.

[23] Bagnold, R. A., 1941, *The Physics of Blown Sand and Desert Dunes*, Methuen.

[24] Bruce, R. W., and Schulzt, J. C., 1977, “Magnus Effect in Saltation,” J. Fluid Mech., **81**(3), pp. 497–512.

[25] Weber, M., 1976, *Pneumatic Conveying of Solids.*

[26] Jones, P. J., and Leung, L. S., 1978, "Estimation of Saltation Velocity in Horizontal Pneumatic Conveying--a Comparison of Published Correlation," *Proceeding of Pneumotransport 4*, Bedford, U.K., pp. 1–12.

[27] Rizk, F., 1976, "Pneumatic Conveying at Optimal Operation Conditions and a Solution of Barth's Equation," *Proceeding of Pneumotransport 3, Paper D4*, Bedford, U.K., pp. 43–58.

[28] Geldart, D., and Ling, S. J., 1992, "Saltation Velocities in High Pressure Conveying of Fine Coal," Powder Technol., **69**(2), pp. 157–162.

[29] Cabrejos, F. J., and Klinzing, G. E., 1994, "Pickup and Saltation Mechanisms of Solid Particles in Horizontal Pneumatic Transport," Powder Technol., **79**(2), pp. 173–186.

[30] Hong, J., and Tomita, Y., 1995, "Analysis of High Density Gas-Solids Stratified Pipe Flow," Int. J. Multiph. Flow, **21**(4), pp. 649–665.

[31] Owen, P. R., 1964, "Saltation of Uniform Grains in Air," J. Fluid Mech., **20**(2), pp. 225–242.

[32] Nalpanis, P., Hunt, J. C. R., and Barrett, C. F., 1993, "Saltating Particles Over Flat Beds," J. Fluid Mech., **251**, pp. 661–685.

[33] Okoli, R. E., 2003, "Wind Tunnel Study on Aeolian Saltation Dynamics and Mass Flow," J. Arid Environ., **53**(4), pp. 569–583.

[34] Nishimura, K., and Hunt, J. C. R., 2000, “Saltation and Incipient Suspension Above a Flat Particle Bed Below a Turbulent Boundary Layer,” J. Fluid Mech., **417**, pp. 77–102.

[35] Soldati, A., and Marchioli, C., 2009, “Physics and Modelling of Turbulent Particle Deposition and Entrainment: Review of a Systematic Study,” Int. J. Multiph. Flow, **35**(9), pp. 827–839.

[36] Kunz, R. F., Yu, W. S., Antal, S. P., and Ettorre, S. M., 2001, “An Unstructured Two-Fluid Method Based on the Coupled Phasic Exchange Algorithm,” *15th AIAA Computational Fluid Dynamics Conference*.

[37] Burns, A. D., Frank, T., Hamill, I., and Shi, J. M., 2004, “The Favre Averaged Drag Model for Turbulent Dispersion in Eulerian Multi-Phase Flows,” *5th International Conference on Multiphase Flow*, pp. 1–17.

[38] Besnard, D. C., and Harlow, F. H., 1988, “Turbulence in Multiphase Flow,” Int. J. Multiph. Flow, **14**(6), pp. 679–699.

[39] Coakley, T. J., 1983, “Turbulence Modeling Methods for the Compressible Navier-Stokes Equations.,” *16th Fluid and Plasmadynamics Conference*, p. 1693.

[40] Suga, K., Craft, T. J., and Iacovides, H., 2006, “An Analytical Wall-Function for Turbulent Flows and Heat Transfer Over Rough Walls,” Int. J. Heat Fluid Flow, **27**(5), pp. 852–866.

[41] Ranz, W. E., and Marshall, W. R., 1952, “Evaporation from Drops,” Chem. Engng. Prog., **48**(3), pp. 173–180.

[42] “NIST Chemistry WebBook, SRD 69,” I. P. f. Nitrogen, Ed., Natl. Inst. Stand. Technol.

[43] 2018, “Nitrogen - Prandtl Number,” Eng. ToolBox, **2020**.

[44] Creysells M., Dupont P., Ould El Moctar A., Valance A., Cantat I., Jenkins J. T., Pasini J. M., and Rasmussen K. R., 2009, “Saltating Particles in a Turbulent Boundary Layer: Experiment and Theory,” J. Fluid Mech., **625**, pp. 47–74.

[45] Carver, M. B., 1984, “Numerical Computation of Phase Separation in Two Fluid Flow,” J. Fluids Eng. Trans. ASME, **106**(2), pp. 147–153.